Variability of eastward currents in the equatorial Atlantic during 1993-2010

Marlos Goes [1,2*], Gustavo Goni[2], Verena Hormann[1,2], and Renellys C. Perez[1,2]

Submitted to Journal of Geophysical Research-Oceans

18- May-2012

[1] Cooperative Institute for Marine and Atmospheric Studies, University of Miami, Miami, FL 33149, USA.

[2] Atlantic Oceanographic and Meteorological Laboratory, National Oceanic and Atmospheric Administration, Miami, FL 33149, USA.

Abstract

We have developed, validated, and applied a synthetic method to monitor the eastward currents in the equatorial Atlantic. This method combines high-density expendable bathythermograph (XBT) temperature data along the AX08 transect crossing the equator at about 23°W with altimetric sea level anomalies (SLAs) to estimate dynamic height fields from which mean properties of the currents and their variability can be estimated on seasonal to interannual timescales. The method is well suited for the surface North Equatorial Countercurrent (NECC) and reproduces the variability of the North Equatorial and Equatorial Undercurrents (NEUC, EUC) with considerable skill. The synthetic method is unable to describe variations of the South Equatorial Undercurrent (SEUC), which is located in a region of low SLA variability. Our results confirm that the NECC shows a strong annual cycle of volume transport, with largest values from July to December. On interannual timescales, there is a positive correlation between the NECC transport, an interhemispheric sea surface temperature (SST) gradient and the southeasterly winds. The NEUC reveals largest transport values (up to 10 Sv) from January to July and is correlated on interannual timescales with SSTs in the Gulf of Guinea and southeastern equatorial Atlantic as well as zonal equatorial winds. The EUC exhibits strong semi-annual and annual variability. This study shows that for a long-term monitoring system both altimetry and XBT data are needed for near-real-time inference of dynamic and thermodynamic properties of the tropical Atlantic current system.

1. Introduction

The tropical Atlantic current system is of great importance for both interhemispheric and west-to-east exchange of heat and nutrients [e.g., Foltz et al., 2003; Brandt et al., 2008], and also impacts the climate and weather in the surrounding continental areas [e.g., Goldenberg et al., 2001; Sutton and Hodson, 2005; Stramma et al., 2005; Brandt et al., 2011], since ocean upper dynamics play an important role in the modes of sea surface temperature variability in this region [e.g., Carton and Huang, 1994; Carton et al., 1996]. In the upper equatorial Atlantic, the main conduit for the interhemispheric water exchange is the western boundary current system of the North Brazil Undercurrent/Current (NBUC/NBC). On its northward path, the NBC partly retroflects eastward and feeds into a system of zonal countercurrents, namely the Equatorial Undercurrent (EUC) along the equator, and three off-equatorial currents, the North Equatorial Countercurrent (NECC), the North Equatorial Undercurrent (NEUC), and to a lesser extent the South Equatorial Undercurrent (SEUC) [e.g., Metcalf and Stalcup, 1967; Cochrane et al., 1979; Peterson and Stramma, 1991; Schott et al., 1995]. Moreover, the eastward equatorial currents play an important role in the global meridional overturning circulation by connecting the western boundary regime to the interior circulation [e.g., Frantantoni et al., 2000], and in the shallow subtropical cells (STCs) by providing water for the off-equatorial eastern upwelling regimes along the African coast, specifically for the Guinea and Angola Domes [e.g., Hisard and Henin, 1987; Zhang et al., 2003; Marin et al., 2003; Hua et al., 2003; Schott et al., 2004; Doi et al., 2007].

The primary equatorial branch of the STCs is the EUC, which is unique in its dynamics [e.g., Moore and Philander, 1986; Pedlosky, 1988; Wacongne, 1989] and has been found to be linked with the Atlantic zonal mode on interannual timescales [e.g., Goes and Wainer, 2003;

Hormann and Brandt, 2007]. The seasonal cycle of the EUC has been widely analyzed in model simulations [e.g., Philander and Packanowski, 1986; Hazeleger et al., 2003; Arhan et al., 2006; Hormann and Brandt, 2007] which generally agree that the EUC shows two transport maxima in the central part of the basin, one during boreal summer/fall and another during boreal winter/spring. Arhan et al. [2006] suggested that two different dynamic regimes drive the seasonal cycle of the EUC: In boreal summer/fall, the simulated EUC is mostly driven locally by equatorial zonal wind forcing, and is supplied from the ocean interior; in boreal winter/spring, it is driven by remote forcing through the rotational wind component, and is supplied from the western boundary currents. Observational studies, however, have drawn different conclusions, either by showing one sole maximum in late boreal summer/autumn [Hisard and Henin, 1987], or no significant seasonal variations [Weisberg et al., 1987].

Due to its strong surface expression, the NECC has been the most extensively studied of the three eastward off-equatorial currents. The NECC is mainly located between 3°-10°N [e.g., Garzoli and Katz, 1983; Richardson and Walsh, 1986], and splits seasonally into two discernible cores that are dynamically linked to the widening of the zonal wind stress band [Urbano et al., 2006]. The seasonal variability of the NECC is strongly tied to the migration of the Intertropical Convergence Zone (ITCZ) [Katz and Garzoli, 1982; Katz, 1987; Garzoli and Richardson, 1989; Garzoli, 1992]. In addition to local wind stress curl and Rossby waves from the eastern basin [e.g., Garzoli and Katz, 1983; Katz, 1987; Garzoli and Richardson, 1989], wind stress fluctuations in the equatorial band have been found to play an important role in driving the seasonal cycle of the NECC [Yang and Joyce, 2006]. The NECC also exhibits considerable year-to-year variability [e.g., Katz, 1993; Fonseca et al., 2004] and Hormann et al. [2012] recently showed that its interannual variability is linked to the two dominant tropical Atlantic climate modes.

The variability of the off-equatorial undercurrents (OEUCs), though, is still not well understood. This is mostly related to observational constraints, since the OEUCs are weaker, diffusive, and highly variable on intraseasonal timescales due in large part to tropical instability wave (TIW) activity [Johnson and Moore, 1997; Rowe et al., 2002; Jochum et al., 2003; Jochum and Malanotte-Rizzoli, 2004]. The OEUCs are located below the thermocline, coincident with the equatorial thermostad, at about ±3°–6° of latitude [Cochrane et al., 1979]. The SEUC is mostly fed by internal recirculations [Schott et al. 1995, 1998], and according to Reverdin et al. [1991], its seasonal cycle at 30°W is characterized by a transport maximum in boreal fall and a minimum in boreal spring. Close to its origin, observations show that the SEUC flow consists of large standing meanders [Fischer et al., 2008]. The NEUC is weaker than the SEUC, and more variable due to enhanced TIW activity in the northern hemisphere [e.g., Foltz et al., 2004b; Athie and Marin, 2008]. For instance, Schott et al. [2003] analyzed an average of 13 shipboard sections at 35°W, and stated as uncertain the existence of the NEUC. Moreover, the separations between the NEUC and EUC in the western part of the basin [e.g., Bourlès et al., 1999; Goes et al., 2005] and the NEUC and NECC in the central part of the basin [Brandt et al., 2010] are not very distinct.

All the eastward currents in the equatorial Atlantic are modified by wind forcing and by oceanic mesoscale phenomena, such as TIWs [e.g., Düing et al., 1975; Weisberg and Weingartner, 1988; Menkes et al., 2002; Grodsky et al., 2005] that can alias estimates of seasonal and interannual variability obtained from observational systems that are not continuous in time, posing a significant sampling challenge. An existing observational system that can potentially resolve the short spatial and temporal scales, and allow for quantification of the seasonal to interannual variability of the eastward currents is satellite altimetry. Although upper-ocean currents in the tropical Atlantic having very weak sea surface height signatures cannot be resolved from surface topography fields alone [Goni and Baringer, 2002], a relationship between certain current features and their characteristic sea surface height signatures can be established to overcome this challenge. This can be achieved by combining altimetry with other observational platforms, such as high-resolution hydrographic data. Therefore, a reliable monitoring system for the region requires complementary platforms in order to produce details of the spatio-temporal variability [Goni and Baringer, 2002].

The goal of this study is to quantify the variability of the eastward currents in the equatorial Atlantic during 1993-2010, and determine their properties, such as transport, velocity, and location. Specifically, we focus on the seasonal to interannual signatures of the NECC, EUC, and OEUCs manifested in the observations. To accomplish this goal, we consider a monitoring system that relies upon data from the cross-equatorial High Density eXpendable BathyThermograph (HD XBT) transect AX08 during 2000-2010, and use satellite altimetry observations to synthetically quantify the variability of the eastward currents in the equatorial Atlantic for the 1993-2010 period. The HD XBT project has been active for over 20 years, and aims at sustainably measuring physical properties of the upper ocean with mesoscale resolution. Its high spatial data resolution and repeated sampling of the region enable assessment of upper-ocean temperature and heat storage variability, and permit characterizing of the variability of the major geostrophic currents.

This paper is structured as follows: First we describe in detail the data to be used (Section 2) and introduce the synthetic methodology (Section 3); in Section 4, we validate the synthetic method, apply it to examine the seasonal and interannual variability of the eastward equatorial currents, and analyze the surface response and forcings linked to this variability. Discussion, conclusions, and recommendations for further development of the methodology are provided in Section 5.

2. Data

This work mainly uses two observational platforms to infer the variability of the eastward currents in the equatorial Atlantic: a high-density XBT transect and satellite altimetry. Specifications for each of these datasets, as well as for additional data used in the analysis are given below.

a) Hydrographic data

The temperature data used in this study are from 39 realizations of the AX08 XBT transect, which is carried out between Cape Town and New York City and crosses the equator at about 23°W (Figure 1a). The first section was obtained in December 2000, and an average of four transects per year has been achieved since 2002. Approximately 200-300 XBTs are deployed during each transect realization, with a nominal spacing of 25 km between casts in the tropics and a maximum depth of roughly 800 m.

In order to study the variability of the eastward equatorial currents, we restrict the observations to a region with similar dynamic characteristics. We define a criterion that selects the sections whose mean longitude lies within the 68 percentile around their median value between 10°S-10°N (Figure 1b). The median longitude of the transect, which is about 40° oblique with respect to a true meridional section, is approximately 23°W (Figure 1a).

Additionally we exclude the September 2004 section because its derived surface dynamic height shows an offset in comparison to the other sections. The applied constraints reduce the number of transects from 39 to 31, but assures that we are working with comparable data.

XBT measurements are performed by sampling temperature and the time of descent of the XBT probes. The elapsed time of descent is converted to depth by applying a fall rate equation [Hanawa et al., 1995]. Individual temperature profiles are linearly interpolated onto a 2 m grid. The data are quality controlled by excluding the outlier profiles, chosen as the profiles whose both forward and backward horizontal gradients of the surface dynamic height lie outside the three standard deviation range of all profiles. Next, the sections are horizontally interpolated to a 25 km resolution in latitude, using an optimal interpolation scheme based on a Gaussian correlation function with a decorrelation length scale of 200 km and a low noise-to-signal ratio of 0.01. Salinity is inferred from the temperature profiles using climatological temperature-salinity (T-S) relationships extracted from the World Ocean Database (WOD01, Conkright et al. [2002]). In the mixed layer, salinity profiles are extrapolated using a slab-layer approximation (Figure 2c, d), which is a standard approximation to overcome the non-unique characteristic of the T-S relationship in the tropical surface waters [Schott et al., 1998; Goes et al., 2005]. The differences between in-situ and climatological salinity have been shown to be of the order of 0.3-0.4 psu, and the resulting uncertainty to be among the largest contributors to the dynamic height error, with differences as large as 5 cm [Goni and Baringer, 2002].

Typical examples of temperature and salinity distributions along the AX08 section in boreal winter and summer are shown in Figure 2. This region is characterized by a warm well-mixed layer in the top 100 m, followed by a sharp temperature gradient of approximately 0.1°C/m that marks the upper thermocline. The waters to the north and south of the displayed domain are characterized by high salinity values at around 100 m, within the upper thermocline waters. These high salinity waters are characteristic of the Subtropical Underwater (SUW). SUWs are formed in the subtropics and advected equatorward by the North and South Equatorial Currents. Underneath the SUW is the central water (CW), characterized by a nearly straight line in the T-S space [e.g., Stramma and England, 1999]. The CW forms the thermostad between 12-15°C found in the equatorial region [Reverdin et al., 1991], which is more pronounced in the southern hemisphere between 5°S and the equator at around 200 m depth (Figure 2), and coincides with the position of the OEUCs [e.g., Cochrane et al., 1979; Schott at al., 1995, 1998].

b) Altimetric data

Here we use the AVISO reference ("ref") delayed mode product (http://www.aviso.oceanobs.com) obtained from a multi-satellite mission [Le Traon et al., 1998], which provides gridded, optimally interpolated, and cross-calibrated global coverage of sea level anomalies (SLAs) relative to the 1993-1999 mean. These delayed mode data are continuously available on a 1/3° horizontal grid with weekly temporal resolution since October 1992, and SLA precision of 2 cm [Ducet et al, 2000; Cheney et al., 1994]. In this study, we use data from October 1992-December 2010 and subtract the 2000-2010 mean from the SLA field for consistency with the XBT dataset. We further interpolate SLA linearly onto to the location and time of the individual XBT sections to estimate regression parameters for the synthetic method, and onto the mean AX08 transect to create a hindcast of the currents for the whole altimetric period.

c) Additional data

We use referenced dynamic height from the monthly climatology of the International Pacific Research Center (IPRC) (http://apdrc.soest.hawaii.edu). This dataset is available on a 1° x 1° horizontal grid at 27 depth levels and is derived from Argo floats and altimetry observations, with mean sea level referred to the mean dynamic topography MDT_CNES-CLS09 [Rio et al., 2011].

We perform additional analyses using gridded sea surface temperature (SST) and pseudo-wind stress anomalies with respect to their climatological means. These data are monthly averaged for the considered altimetric period, and interpolated onto a 1° x 1° Mercator grid. The SST data are extracted from the optimum interpolation (OISST-v2) analysis [Reynolds et al., 2002], which is available weekly on a 1° horizontal grid since November 1981. The pseudo-wind stress data are obtained from the cross-calibrated, multi-platform (CCMP), multi-instrument ocean surface wind velocity data set. This product combines data derived from SSM/I, AMSRE, TRMM TMI, Quikscat, and other missions using a variational analysis method to produce a consistent record of ocean surface vector winds at a 25 km resolution and is available since July 1987 [Atlas et al., 2011].

3. Methodology

a) *Velocity calculation*

We calculate the cross-sectional absolute geostrophic currents from horizontal gradients of absolute dynamic height (DH(z)) using the thermal wind relationship. To obtain DH(z), we reference the XBT-derived dynamic height (DH_{XBT}) to the IPRC monthly climatology of absolute dynamic height at 800 m (DH_{IPRC}(800m)) for each XBT transect:

$$DH(z) = DH_{XBT}(z) + DH_{IPRC}(800m) \qquad (1)$$

Although the inclusion of DH_{IPRC}(800m) alters the mean DH significantly, DH gradients are not greatly affected (O(10^{-7}) cm/km change). Geostrophy has an inflection point at the equator and it is necessary to use the equatorial beta approximation, which relies on the calculation of higher order derivatives of the DH(z) near the equator. In this study, we apply the method of Lagerloef et al. [1999] for velocity calculations within ± 3° off the equator, except here we use a 6th order polynomial rather than a 3rd order polynomial.

We further explore the effect of salinity on the steric variability in the XBT data by calculating the thermosteric and halosteric contributions to the total surface dynamic height variability at three different latitudes, 4.5°N, 4.5°S, and the equator (Figure 3). These latitudes roughly coincide with the core of the eastward currents. The calculation of the thermosteric and halosteric contributions is performed using the methodology described by Fofonoff and Froese [1958] and Tabata et al. [1986] in which departures from the mean sea level are estimated in terms of one component by keeping the other component fixed at its annual mean. The sum of the thermosteric and halosteric components is approximately equal to the total steric variability of the XBT data. We illustrate their contributions to the surface dynamic height (DH_0) referenced to 800 m and at all three latitudes (Figure 3). Results indicate that the variability of total DH_0 is largely explained by its thermosteric component, and that the halosteric contribution to the variability of DH_0 is rather small, generally of the order of 1-2 cm. Halosteric effects have a larger contribution to the total DH_0 variability at the equator and 4.5°S (Figure 3b,c), where the total DH_0 variability is small compared to 4.5°N. At those latitudes, the halosteric component accounts for 20-30% of the total variability, while at 4.5°N (Figure 3a), where there is high thermosteric variability with amplitudes of up to 20 cm, only about 10% of the DH_0 variability is due to the halosteric component.

The a priori errors in geostrophic velocity resulting from our methodology include XBT temperature precision of ± 0.1°C (O[1 cm/s]), the use of salinity estimates from climatological T-S relationships (O[5 cm/s]), and the uncertainty in the level of known motion (O[1 cm/s]). An additional error results from the assumption that the cross-sectional geostrophic velocity along an oblique transect (Figure 1a) is approximately equal to the zonal geostrophic velocity estimated from a meridional transect. This error has been previously quantified in a similar region as smaller than 10% (O[4 cm/s]) by Reverdin et al., [1991]. We performed tests with satellite altimetry data (not shown here) and concluded that 10% error is a conservative estimate due to the large random variability in the region. Assuming the errors above are random and uncorrelated, their total contribution would result in an error of ± 6.5 cm/s, which is on the order of or smaller than the intrinsic mesoscale variability of the region [e.g., Grodsky et al., 2005; Brandt et al., 2006]. Therefore, the standard errors of the monthly averages will be used as a confidence interval for our calculations. Near the equator, the beta plane approximation introduces errors up to one order of magnitude greater (O[10 cm/s]) than the other components, and this caveat has to be taken into consideration in the analysis of the EUC results.

b) *Synthetic method*

Altimetry data is used here along with those of other observational platforms to provide a broader four-dimensional (i.e., spatial and temporal) coverage of the tropical Atlantic. Several studies have combined altimetric and hydrographic data to infer properties of the upper ocean, such as velocity, temperature, and salinity [e.g., Gilson et al., 1998; Ridgway, 2002; Phillips and Rintoul, 2002].

Here, we apply a synthetic method to produce a hindcast of the velocity and density fields along the mean AX08 transect position (red line in Figure 1a). Since we are interested in velocity sections along isopycnal layers, we seek as predictands potential density (σ_θ) and DH from the surface to 800 m and use altimetric SLA data as predictors. To determine the relationship between the predictors and predictands, we first calculate the absolute DH (Equation 1) for the 31 selected XBT sections. Anomalies of σ_θ and DH (σ'_θ and DH', respectively) are calculated by subtracting a mean annual field, defined by the mean WOD01 density field along the mean section and the mean dynamic height field of all sections. For the latter, we first calculate monthly averages to reduce potential sampling biases toward any specific month (Figure 1c). These results are largely insensitive to the mean fields since only a constant is subtracted from the temporal fields, but removing a mean is known to also reduce the variance of residuals in a linear regression. Anomalies of DH_0 (DH'_0) are linearly regressed onto DH' and σ'_θ as a function of latitude and depth. Finally, the DH'_0 is linearly regressed onto SLA forming the link between the altimetric and hydrographic observations. The DH'_0 and SLA are well correlated (Figure 4d), with $R^2 = 0.75$ (the R-squared coefficient corresponds to the squared correlation in a simple linear regression), a root mean square error of RMSE = 2.40 cm, and a negligible intercept. This strong and unbiased relationship between the two variables shows that the SLA captures well the baroclinic structures in the region, especially the first mode [Gilson et al., 1998; McCarthy et al., 2000; Guinehut et al., 2006]. The highest SLA variance occurs between 5°-10°N, coinciding with the highest SLA gradients which are closely related to the dynamics of the NECC. Less variability is observed south of the equator, which may be due to compensating effects in the water column [Mayer et al., 2001]. The differences found here between SLA and DH'_0 can arise from a number of factors, such as temporal and spatial sampling, incomplete removal of tides, as well as barotropic flow variations and changes in the entire depth of the ocean [Rintoul et al., 2002].

Here we use the temporal correlation between DH'_0 and the predictands at each depth and latitude as an indicator of the skill of this method to monitor the variability of the predictands DH' and σ'_θ (Figure 5). As expected, these correlations are predominantly positive for DH' and negative for σ'_θ since dynamic height is calculated from specific volume anomalies, which are inversely related to density [Pond and Pickard, 1983]. Apart from their sign, both fields show similar relationships, with highest correlations in the upper 200 m of the water column, and decreasing correlation values with depth. In certain latitudes, such as in the vicinity 5°N, high correlations ($R \approx 0.8$) can reach depths of 800 m, similar to values encountered in the North Pacific [Roemmich and Gilson, 2001].

4. Results

4.1 Identification of upper and lower layer currents.

The central tropical Atlantic has a very characteristic seasonal variability of the surface dynamic height. During December through May, DH_0 is nearly flat between 10°S-10°N, implying small surface geostrophic velocities (Figure 6a, b). From June to November (Figure 6c, d), the DH_0 gradients are larger north of 5°N and as a result the NECC core is stronger and well defined. A second NECC core develops in late boreal summer/early boreal fall around 8°-10°N (Figure 6c, d) and the NECC shows a maximum double peak structure during boreal fall (Figure 6d) which is in agreement with previous results [e.g., Didden and Schott, 1992; Urbano et al., 2006]. Results obtained indicate that there is often a connection between the surface NECC and the flow in the thermocline layer, when the NEUC can be found as a lobe attached to the southern NECC branch. During boreal spring (Figure 6b), however, the NEUC is clearly detached from the NECC. A signature of the NEUC on the σ_θ = 26.8 kg m^{-3} isopycnal is observed at approximately 5°N, but it does not show a very sharp gradient [c.f., Bourlès et al., 2002; Schott et al., 2003]. In contrast, the potential density structure at about 4°-5°S, where the SEUC is located at around 200 m, exhibits a very distinguished southward elevation of the σ_θ = 26.8 kg m^{-3} surface. This is an indication that the meridional pressure gradient plays an important role in SEUC dynamics. The isopycnal signature of the SEUC and its well-defined core are visible throughout the year, indicating that the SEUC is a permanent feature in the tropical Atlantic. The EUC core is generally located south of the equator and between the surface and 100 m, with eastward flow typically between 2.5°S and 2.5°N, (Figure 6).

We define the location of the equatorial eastward currents by assigning a latitudinal band to each of them (Table 1), similar to the bands used in previous studies [e.g., Hüttl-Kabus and Böning, 2008]: The NECC is defined between 3°-10°N, the NEUC between 3°-6°N, the SEUC between 3°-6°S, and the EUC between 2.5°S and 2.5°N. We further characterize these currents by selecting isopycnal layers to define their vertical boundaries: an upper or surface layer from the surface to σ_θ = 24.5 kg m^{-3}, and a lower or thermocline layer between σ_θ = 24.5 - 26.8 kg m^{-3} [e.g., Schott et al., 1998]. The NECC is restricted to the upper layer, and the OEUCs to the lower layer. The EUC has significant contributions in both layers, thus it is considered to occupy both the surface and lower layers.

4.2 Synthetic method validation

We validate the synthetic method by comparing the transports of the eastward equatorial currents estimated from the 31 XBT transect realizations with their synthetic counterparts

(Figure 7). The agreement between the synthetic and XBT transport estimates is high for the NECC (Figure 7a, b), with RMSE = 0.72 Sv. A strong linear relationship is found between the two estimates, with a corresponding linear-correlation coefficient of $R^2 = 0.95$. The EUC (Figure 7g, h), which has transport contributions from the upper and lower layers, shows a moderate-to-high agreement between the synthetic and XBT transport estimates ($R^2 = 0.55$, RMSE = 7.0 Sv). Regarding the OEUCs, the synthetic method has considerable skill for the NEUC ($R^2 = 0.34$), but the transports using XBT data are generally higher than the synthetic ones (Figure 7c, d), with RMSE = 1.2 Sv. The synthetic method is able to reproduce a comparable mean SEUC transport of 7 Sv to the one derived from the XBT data. However, the method fails to reproduce the SEUC transport variations (Figure 7e), with low correlations between the synthetically-derived and XBT-derived SEUC transports ($R^2 = 0.04$, RMSE = 0.43 Sv), and the variance of the synthetically-derived SEUC transport barely resembles the ones from hydrography (Figure 7e). Due to the low agreement between the two SEUC transport estimates, analysis of the variability of the synthetic fields will focus on the NECC, NEUC, and to a lesser extent the EUC.

4.3 Seasonal variability of the eastward equatorial currents

Here we analyze the seasonal variability of the NECC, NEUC, SEUC, and EUC along the AX08 transect in terms of cross-sectional volume transport, core velocity, and core latitude using their monthly average values. The selected 31 AX08 temperature sections provide high-resolution coverage of the central tropical Atlantic for all months except February (Figure 1c). We apply to the XBT-derived quantities a previously used methodology [Foltz et al., 2004a] to estimate monthly means and variances of transport, core velocity, and position of the currents. This method fits the first two harmonics (i.e., annual and semi-annual) to the data in a least squares fashion. It accounts for observational uncertainties by calculating a diagonal covariance matrix, with each diagonal term corresponding to a month, calculated as the sum of the fitting residual error and the observational error given by the standard deviation of each month. Fitting the first two annual harmonics to the data filters a large fraction of the mesoscale signal.

a) NECC

The hydrographic estimates show a strong annual cycle of the NECC, which alone represents 58% of the transport, 41% of the maximum velocity, and 52% of the position variances (Table 2). Earlier analyses based on drifter data also show a dominant contribution, as high as 80%, of the annual cycle for the off-equatorial surface currents [e.g., Richardson and Walsh, 1986; Lumpkin and Garzoli, 2005]. The NECC (Figure 8a, i) reaches its southernmost position in boreal spring (~3°-4°N), concurrent with its lowest transport (~1 Sv), and its northernmost position (~7°-9°N) during boreal fall, coincident with its highest transport (~10-11 Sv). The NECC core velocity shows a similar pattern, with lowest values (~10-20 cm/s) in boreal spring and maximum values (~55 cm/s) in boreal fall (Figure 8e). This seasonal variability of the NECC agrees with previous observational findings [e.g., Richardson et al., 1992], and it is linked to the north-south migration of the ITCZ [Katz and Garzoli, 1982; Katz, 1987; Garzoli and Richardson, 1989; Garzoli, 1992; Fonseca et al., 2004], which is near the equator during boreal spring and farthest north during boreal summer.

The estimates using the synthetic method for the comparable 2000-2010 period (blue lines in Figure 8a, e, i) follow closely the estimates from hydrography. As the synthetic estimates are averaged using a much longer time series, and the hydrographic data are subject to higher influence of mesoscale effects due to sparse temporal sampling (Figure 1c), differences are expected and the synthetic method generally shows higher explained variances by the annual cycle (Table 2). The synthetically-derived core velocity time series (Figure 8e) reveal stronger semi-annual variability during 1993-2000 (blue lines) compared to the 2000-2010 decade (green lines) and hydrographic data (red lines). Additional characteristics of how the NECC transport varies over time can be retrieved by applying a wavelet transform [Torrence and Compo, 1998] to the NECC transport time series for the whole altimetric period (Figure 9a). This analysis confirms that the annual cycle of the NECC is the strongest signal in the synthetically-derived transport time series. Moreover, the energy of the annual period shows intermittent increases and a prominent semi-annual signal is observed during an event in 1998-1999, when there is a strong peak in the NECC transport time series. The latter might be related to a strong wind stress curl anomaly in the western tropical Atlantic during that period, which has been previously described [Fonseca et al., 2004]. Mechanisms related to the interannual variability of this current are explored in Section 4.2.

b) NEUC

The NEUC shows higher transport values during boreal spring (Figure 8b), when its transport ranges from 5-10 Sv, and lower transports (~2-3 Sv) in boreal fall. Compared to the seasonal cycle of NECC transport (Figure 8a), the NEUC bears an almost inverse relationship with the NECC, and therefore with the ITCZ. The overlapping of the positions of these two currents from April to May (Figures 8i, j) suggests that the NECC may partly contribute to the NEUC flow during this period. The annual cycle dominates the XBT transport variability (explained variance: 63%), whereas the semi-annual cycle only explains 1% of the variance (Table 2). The seasonal variability of NEUC location (Figure 8j) resembles its transport variability, in that a more southward position (~3.5°-4°N) occurs during boreal spring at the time of higher transport. The NEUC core velocity (Figure 8f) exhibits a relatively strong semi-annual cycle (explained variance: 35%, Table 2), with maximum speed of about 25 cm/s during boreal winter and summer and smaller core velocity of about 10-15 cm/s in September-October, revealing that the NEUC is present year-round in this latitude band. The synthetic estimates broadly agree in magnitude with the XBT measurements and may indicate some changes between the 1990s and 2000s. The wavelet analysis performed for the whole altimetric period indicates a possible shift in energy from a prevailing semi-annual to an annual variability starting in 1999-2000 (Figure 9b). There are also indications of interannual variability in the NEUC transport, with increased energy centered in 1995, 2001 and 2006. The resemblance between the variability of the zonal winds in the equatorial region (Figure 9d) and the NEUC transport variability is noteworthy, and mechanisms for this variability will be explored in Section 4.2.

c) SEUC

The XBT-derived transport of the SEUC (Figure 8c) is weaker (~6 Sv) from July to September, in agreement with Reverdin et al. [1991], and it is also reduced in January (~5 Sv). Maximum transport values are found from October through December, reaching up to 10 Sv, and mean transport is about 7-8 Sv, in good agreement with previous estimates [Brandt et al., 2006; Fischer et al., 2008]. The semi-annual harmonic component is dominant and explained variances are 90% and 92% for transport and core velocity (Table 2), respectively, which is consistent with model studies [e.g., Hüttl-Kabus and Böning, 2008]. The core velocity is about 28 cm/s in May/June and October, and 20 cm/s in August (Figure 8g). Fischer et al. [2008] reported a weaker mean SEUC velocity of 13.4-17.9 cm/s in central tropical Atlantic, but departures from this mean of up to 50 cm/s have been observed in its core. The mean position of the SEUC is about 4.5°±0.5°S and although small, its position variability (Figure 8k) follows closely its transport variability, in that higher transports are associated with a more northern position and vice versa.

d) EUC

The XBT and synthetic estimates agree well in that the EUC near 23°W is located mostly south of the equator, between 1°S±1° (Figure 8l). Despite the relatively small seasonal variability of the EUC location, there are indications of a more southward position during boreal fall/winter. The core velocity (Figure 8h) derived from XBT data is generally higher than from the synthetic method, between 40-80 cm/s, and shows strong annual variability (explained variance: 72%, Table 2), whereas the synthetic core velocity estimates range from 30 to 50 cm/s, and exhibit a more semi-annual periodicity. The XBT estimates are comparable to direct velocity observations of the EUC, which show mean values of about 70-80 cm/s [e.g., Giarolla et al., 2005; Brandt et al., 2006, 2008]. The EUC transports (Figure 8d) derived from both hydrographic and synthetic estimates exhibit strong semi-annual variability (i.e., explained variances between 40-68%, Table 2), with lower values during boreal summer and winter, and higher values during boreal spring and late summer-early fall. The wavelet analysis (Figure 9c) of the synthetic transport confirms the strong semi-annual variability of the EUC, in agreement with results from previous model studies of the central equatorial Atlantic [e.g., Arhan et al., 2006; Hormann and Brandt, 2007]. The high variability of the XBT estimates in some months (see for instance the error bars of transport and core velocity during July in Figures 8d, h) are an artifact of the equatorial beta approximation for specific monthly density structures and need to be interpreted carefully.

4.4 Interannual variability of the synthetic transports of the eastward currents

In this section, we investigate the interannual signature of the NECC and NEUC on SST and surface wind stress using statistical tools. We restrict our analysis to the NECC and NEUC transports because the synthetic method does not provide good estimates of the SEUC variability and because we do not expect that the equatorial beta approximation can produce reliable estimates of the EUC transport variability on interannual timescales. We use here monthly transport anomalies relative to the monthly climatology, with the intent of reducing the influence of eddy variability on these currents. Furthermore, we perform correlation analyses of the monthly NECC and NEUC transport anomalies with the gridded monthly anomalies of both SST and pseudo-wind stress. Correlation analyses are performed in the tropical Atlantic region for the 1993-2010 period, taking only statistically significant values into account ($p < 0.05$). In this analysis, all data are standardized by subtracting their mean and dividing by their standard deviation and low-pass filtered with a 5-month moving average.

a) NECC

The correlation between the NECC transport and SST anomalies (SSTA) for the altimetric period produces a distinct pattern in the form of an anomalous interhemispheric SST gradient (Figure 10a), with positive phase just north of the equator in the ITCZ region, centered at approximately 2°N, 30°W, and extending northeastward, and negative phase in the central south of the domain, centered at about 20°S, 17°W. The corresponding correlation with pseudo-wind stress anomalies indicates an anomalous strengthening of the southeasterly trades, with largest magnitude in the western equatorial region where winds are also strongest. This pattern is reminiscent of the Atlantic meridional mode [e.g., Chang et al., 2006, and references therein], which is believed to be driven by the wind-evaporation-SST (WES) feedback mechanism involving interactions between SST changes and wind-induced latent heat fluxes [Xie and Philander, 1994; Chang et al., 1997]. A similar pattern has also been found for the NECC in a recent study using complex empirical-orthogonal-function analysis of surface drifter data [Hormann et al., 2012].

A SSTA gradient index can be defined by subtracting area averages within the northern (35°W-17°W/0°-7°N) and southern (30°W-15°W/11°S-23°S) boxes marked in Figure 10a. The correlation between the monthly NECC transport anomalies and the SSTA index is significant (R = 0.43), with maximum correlation at zero lag. A meridional wind-stress (y-wind) index, computed in the northern box described above, which focuses on the variability near the central equatorial region, shows a maximum positive correlation of R = 0.44, with the NECC lagging the wind strengthening by one month. This relationship indicates that there is a fast response of the NECC and SST to wind anomalies that might be explained by either the fast adjustment time of the ocean through equatorial waves [e.g., Ma, 1996] or by anomalies simply connected to a strengthening of the surface NBC retroflection.

b) NEUC

The pattern arising from the correlation between the NEUC transport with SST and wind stress anomalies (Figure 11) can be described as follows: Negative SST coefficients prevail in the northeastern part of the basin, while positive correlations are found along the equator and off the southwestern African coast. In addition, the trades are reduced in the western to central equatorial Atlantic and southwesterly wind anomalies prevail over the Gulf of Guinea. The obtained interhemispheric SST pattern suggests a relation to the Atlantic meridional mode, and the equatorial SST pattern also indicates a relation to the zonal mode [e.g., Chang et al., 2006, and references therein], further supporting the previously proposed link between these two modes [Servain et al., 1999; Foltz and McPhaden, 2010]. The wind stress anomalies also agree with proposed mechanisms in that this anomalous SST pattern shifts the ITCZ south [Moura and Shukla, 1981], reinforcing the positive SST anomaly along equator [Foltz and McPhaden, 2010].

Previous studies that used virtual Lagrangian floats have shown that the NEUC provides waters for the upwelling in the Guinea Dome and equatorial regions [Stramma et al., 2005; Hüttl-Kabus and Böning, 2008]. Results obtained here agree that the NEUC transport anomalies are negatively correlated with SSTAs and northeasterly wind anomalies in the Guinea Dome region (Figure 11a), which are consistent with an increased coastal upwelling in this region. As for the NECC, we create an interhemispheric SST index and a meridional wind stress index, and relate these indices to the NEUC transport. We consider here the difference between SSTA in the Guinea Dome region (10°-25°N/15°-35°W) and in the southeast Atlantic (8°S-5°N/30°W-10°E) as well as the meridional wind stress average over the Guinea Dome region. We find that the maximum correlation between the NEUC transport with the indices of SST and wind to be R = -0.51 and R = -0.32, respectively, both at zero lag (Figure 11c).

5. Discussion and Conclusions

In the present study, we have used a combination of high-density quarterly AX08 XBT transect and altimetric data to investigate the variability of the eastward surface and subsurface currents in the equatorial Atlantic. The high spatial resolution of the hydrographic data and its repeated sampling of the region enabled us to assess the dynamic and thermodynamic properties of the upper ocean, and permit the characterization of the seasonal cycle of major geostrophic zonal currents such as the NECC and NEUC. However, due to strong regional intraseasonal variability generated by eddy effects and the passage of TIWs, it is hypothesized that it would be necessary to carry out a high number of sections for one to be able to produce a good statistical estimate of the seasonal cycle of these currents using hydrography only. For instance, out of the 31 analyzed XBT sections only one realization is available for January, May, and June, and no section is yet available for February.

Combining altimetry and XBT data by a synthetic methodology reproduces the main surface and subsurface features along the equatorial AX08 XBT transect, which could not be obtained by altimetry alone, overcoming the sampling restrictions, and producing better estimates of the long-term average of the currents properties. The best performance of the synthetic methodology for the equatorial AX08 region resides in the upper 200-300 m of the water column, where temporal correlations between SLA and anomalies of density and dynamic height are larger than 0.8.

The seasonal cycle of the eastward equatorial currents derived from our analyses are in good agreement with previous works [e.g., Richardson and Reverdin, 1987; Peterson and Stramma, 1991; Bourlès et al., 2002; Hormann and Brandt, 2007]. The NECC exhibits a strong seasonal cycle, with transports ranging from 1 to 11 Sv and maximum speed greater than 50 cm/s. Its seasonal variability is related to the migration of the ITCZ [e.g., Garzoli and Richardson, 1989; Fonseca et al., 2004], with stronger transport positively correlated to a northward shift of the ITCZ. On interannual timescales, the NECC transport is found to be linked to a strengthening of the southwesterly trades and a positive interhemispheric SST gradient pattern (i.e., warmer tropical North Atlantic and colder tropical South Atlantic), consistent with

Hormann et al. [2012]. The NECC strengthening associated with such an interhemispheric SST gradient might act as a positive feedback, since it would increase the eastward transport of warmer western waters toward the region of the SST maximum gradient. Previous studies have shown that this tropical Atlantic SST pattern is influenced by the Atlantic Multidecadal Oscillation and the North Atlantic Oscillation, and teleconnections from the eastern Pacific [e.g., Enfield and Mayer, 1997; Czaja et al., 2002]. The recent decrease in sulphate aerosol emissions over the North Atlantic might be associated with a SST increase there and a consequent northward trend of the ITCZ [Chang et al., 2011]. Our results indicate a possible recent strengthening of the climatological NECC of the order of about 1 Sv in the 2000s (Figure 8a), but this value is small compared to the year-to-year NECC variability.

The dominant annual cycle of the NEUC is characterized by stronger transports from January to July (up to 10 Sv), which is in opposite phase to the NECC transport cycle. The NEUC core is located between 4°N-6°N, with maximum velocities of about 30 cm/s in June-July. Synthetic estimates of the NEUC transport suggest that the semi-annual variability used to be stronger during the 1990s, that there was a shift to a stronger annual periodicity since 2000, and that throughout the record there has been an interannual modulation of the annual variability. The latter is also in agreement with anomalous zonal wind stress variability in the central-western equatorial Atlantic (Figure 9b, d) as well as an index of the Atlantic meridional mode [Foltz et al., 2012]. Our results further indicate that the interannual variability of the NEUC transport is statistically related to the upwelling in the equatorial Atlantic and the variability in the Guinea Dome region. Such a link between the NEUC and the Guinea Dome has long been proposed [e.g., Voituriez, 1981; Schott et al., 2004], since the uplifting of the thermal structure in the dome extends much further down than the thermocline. The strong upwelling in this region is, for instance, related to the outcropping of the σ_θ = 24.5 kg/m^3 isopycnal. The underlying mechanism of this relationship might be that a cooler Guinea Dome and warmer equatorial region increase the north-south density gradient in the NEUC region, and strengthen its core. Some model studies in the Pacific indeed suggest that the coastal upwelling in the eastern side of the basin can drive the variability of such a current [e.g., McCreary et al., 2002].

The NEUC and NECC exhibit an inverse relationship in transport variability on interannual timescales. Both are linked to the variability of the cross-equatorial wind stress, but the NECC is strengthened in association with increased southwesterly winds whereas increases in the NEUC are associated with reduced southwesterly winds. The interannual modes of tropical Atlantic variability are strongly tied to their seasonal cycle [Nobre and Shukla, 1996, Servain et al., 1999], which can also explain why the inverse relationship between the NEUC and NECC transports also holds for seasonal timescales. Our results suggest that the NECC contributes to the NEUC, especially during the boreal spring, when the NECC is located further south.

The SEUC calculated from hydrography is located on average at about 4.5°S and exhibits a rather weak seasonal cycle, with mean transport of about 7 Sv, higher values from October to December, and a secondary peak during May-June. Velocities during the stronger months are of the order of 25-30 cm/s. Although the synthetic method produced a comparable SEUC mean flow, it failed to describe its variability. The limited ability of our methodology to capture the SEUC is a consequence of the somewhat weak variability of SLA in the southern tropical Atlantic (Figure 1a), and the resulting surface signature of the current is masked by compensating effects in the water column (Figure 6). The compensating effects can be explained, for example, by buoyancy and wind forcing components of the same magnitude and opposing signs [Mayer et al., 2001]. Therefore, regular hydrographic sampling is particularly important for monitoring the SEUC.

The EUC can be resolved by the equatorial beta approximation using hydrographic data. The seasonal cycle of the EUC is well explained by the annual and semi-annual harmonics, with peaks in boreal fall and spring indicating a relatively strong semi-annual component. The mean EUC derived from XBT data transports 24 Sv, with a corresponding core velocity of 56 cm/s, whereas the synthetic EUC exhibits a mean transport of 14 Sv and core velocity of 34 cm/s. Based on 11 cross-equatorial ship sections taken in the central equatorial Atlantic, Brandt et al. [2006] reported a mean EUC transport of 13.8 Sv, and observed mean velocities are of the order of 70-80 cm/s [e.g., Giarolla et al., 2005; Brandt et al., 2006, 2008]. Therefore, we conclude that the modified Lagerloef et al. [1999] equatorial beta approximation applied to dynamic height estimates generates a weaker, more diffuse, and wider EUC compared to direct velocity observations.

Results from this study are subject to specific caveats that provide avenues for future research: First, we use a simple statistical method to infer the relationship between surface height and ocean properties at depth. Using an improved statistical method may allow for including additional information, such as latitudinal cross-correlation between and autocorrelation of the residuals at depth, as well as the use of additional constraints derived from co-located observations. Second, we use climatological values of salinity calculated from a mean T-S relationship at each location, and also climatological values of the absolute dynamic height at 800 m. Available observations from the Argo network, for example, could reduce errors in the methodology. However, these observations are mostly restricted to the last 5-6 years. Third, along-track altimetry data might provide better agreement between altimetric SLA and hydrography-based dynamic height at the surface, since it is less smoothed by optimal interpolation procedures than the gridded altimetry product used here. Finally, high-resolution modeling can fill gaps in the observational results and confirm the robustness of our conclusions in a dynamically consistent fashion.

Acknowledgements

The authors would like to thank Greg Foltz, Rick Lumpkin, and Molly Baringer for insightful discussions, and George Halliwell for helpful comments. This research was carried out under the auspices of the Cooperative Institute for Marine and Atmospheric Studies (CIMAS), a cooperative institute of the University of Miami and the National Oceanic and Atmospheric Administration (NOAA), cooperative agreement #NA17RJ1226. The XBT transects are funded by NOAA's Climate Program Office and the authors acknowledge the effort of ship crews and logistical personnel.

References

Arhan, M., A. M. Treguier, B. Bourlès, and S. Michel (2006), Diagnosing the annual cycle of the Equatorial Undercurrent in the Atlantic ocean from a general circulation model, J. Phys. Oceanogr., 36, 1502-1522.

Athie, G., and F. Marin (2008), Cross-equatorial structure and temporal modulation of intraseasonal variability at the surface of the Tropical Atlantic ocean, J. Geophys. Res., 113, C08020, doi:10.1029/2007JC004332.

Atlas, R., R. N. Hoffman, J. Ardizzone, S. M. Leidner, J. C. Jusem, D. K. Smith, and D. Gombos (2011), A cross-calibrated, multiplatform ocean surface wind velocity product for meteorological and oceanographic applications, Bull. Amer. Meteor. Soc., 92, 157-174. doi: 10.1175/2010BAMS2946.1.

Bourlès, B., Y. Gouriou, and R. Chuchla (1999), On the circulation in the upper layer of the western equatorial Atlantic, J. Geophys. Res., 104, C9, 21,151-21,170.

Bourlès, B., M. D'Orgeville, G. Eldin, Y. Gouriou, R. Chuchla, Y. DuPenhoat, and S. Arnault (2002), On the evolution of the thermocline and subthermocline eastward currents in the Equatorial Atlantic, Geophys. Res. Lett., 29(16), 1785, doi: 10.1029/2002GL015098.

Brandt, P., F. A. Schott, C. Provost, A. Kartavtseff, V. Hormann, B. Bourlès, and J. Fischer (2006), Circulation in the central equatorial Atlantic: Mean and intraseasonal to seasonal variability, Geophys. Res. Lett., 33, L07609, doi:10.1029/2005GL025498.

Brandt, P., V. Hormann, B. Bourlès, J. Fischer, F. A. Schott, L. Stramma, and M. Dengler (2008), Oxygen tongues and zonal currents in the equatorial Atlantic, J. Geophys. Res., 113, C04012, doi:10.1029/2007JC004435.

Brandt, P., V. Hormann, A. Körtzinger, M. Visbeck, G. Krahmann, L. Stramma, R. Lumpkin, and C. Schmid(2010), Changes in the ventilation of the oxygen minimum zone of the tropical North Atlantic, J. Phys. Oceanogr., 40, 1784-1801, doi:10.1175/2010JPO4301.1.

Brandt, P., A. Funk, V. Hormann, M. Dengler, R. J. Greatbatch, and J. M. Toole (2011), Interannual atmospheric variability forced by the deep equatorial Atlantic Ocean, Nature, 473, 497–500, doi:10.1038/nature10013.

Carton, J. A., and B. H. Huang (1994), Warm events in the tropical Atlantic. J. Phys. Oceanogr., 24, 888-903.

Carton, J. A., X. H. Cao, B. S. Giese, and A. M. daSilva (1996), Decadal and interannual SST variability in the tropical Atlantic Ocean, J. Phys. Oceanogr., 26, 1165-1175.

Chang, P., L. Ji, and H. Li (1997), A decadal climate variation in the tropical Atlantic ocean from thermodynamic air-sea interactions, Nature, 385, 516–518.

Chang, P., T. Yamagata, P. Schopf, S. K. Behera, J. Carton, W. S. Kessler, G. Meyers, T. Qu, F. Schott, S. Shetye, S. P. Xie (2006), Climate Fluctuations of Tropical Coupled Systems—The Role of Ocean Dynamics, J. Clim., 19, 20, 2006, 5122-5174, doi:10.1175/JCLI3903.1

Chang, P., Y. Fang, R. Saravanan, L. Ji, and H. Seidel (2006), The cause of the fragile relationship between the Pacific Nino and the Atlantic Nino, Nature, 443, 324-328, doi: 10.1038/nature05053.

Chang, C-Y, J. C. H. Chang, M. F. Wehner, A. R. Friedman and R. Ruedy (2011), Sulfate Aerosol Control of Tropical Atlantic Climate over the Twentieth Century, J. Clim., 24, 2540-2555, Doi: 10.1175/2010JCLI4065.1.

Cheney, R., L. Miller, R. Agreen, N. Doyle, and J. Lillibridge (1994), TOPEX/Poseidon: The 2-cm solution, J. Geophys. Res., 99, 24,555-24,563.

Cochrane, J. D., F. J. Kelly Jr., and C. R. Olling (1979), Subthermocline counter-currents in the western equatorial Atlantic Ocean, J. Phys. Oceanogr., 9, 724–738.

Conkright, M. E., et al. (2002), World Ocean Database 2001, vol. 1, Introduction, NOAA Atlas NESDIS 42, 159 pp., U.S. Gov. Print. Off., Washington D. C.

Czaja, A., P. van der Vaart and J. Marshall (2002), A diagnostic study of the role of remote forcing in Tropical Atlantic variability, J. of Climate, vol 15, 3280-3290, 2002.

Didden, N., and F. Schott (1992), Seasonal variations in the Western Tropical Atlantic: surface circulation from geosat altimetry and WOCE model results, J. Geophys. Res. C 97 (3), 3529–3541.

Doi, T., T. Tozuka, H. Sasaki, Y. Masumoto, and T. Yamagata (2007), Seasonal and interannual variations of oceanic conditions in the Angola Dome, J. Phys. Oceanogr., 37(11), 2698–2713.

Ducet, N., P.-Y. Le Traon, and G. Reverdin (2000), Global high resolution mapping of ocean circulation from Topex/Poseidon and ERS-1 and -2, J. Geophys. Res., 105 (C8), 19477-19498.

Düing, W., P. Hisard, E. Katz, J. Meincke, L. Miller, K. V. Moroshkin, G. Philander, A. A. Ribnikov, K. Voigt, and R. Weisberg (1975), Meanders and long waves in the equatorial Atlantic, Nature, 257, 280-284, doi:10.1038/257280a0.

Enfield, D. B., and D. A. Mayer (1997), Tropical Atlantic sea surface temperature variability and its relation to El Niño-Southern Oscillation, J. Geophys. Res., 102(C1), 929–945, doi:10.1029/96JC03296.

Fischer, J., V. Hormann, P. Brandt, F. A. Schott, B. Rabe, and A. Funk (2008), South Equatorial Undercurrent in the western to central tropical Atlantic, Geophys. Res. Lett., 35, L21601, doi: 10.1029/2008GL035753.

Fofonoff, N. P., and C. Froese Fisher, (1958) Program for oceanographic computations and data processing on the eletronic digital computer ALWAC II-E, PSW-1 Programs for properties of sea water. Manuscript Rep. Series, Liminol. Oceanogr., J. Fish. Res. Bd. Canada, 27, 39 pp.

Foltz, G. R., S. A. Grodsky, and J. A. Carton (2003), Seasonal mixed layer heat budget of the tropical Atlantic Ocean. J. Geophys. Res., 108, 3146, doi:10.1029/2002JC001584.

Foltz, G., S. Grodsky, and J. Carton (2004a), Seasonal salt budget of the northern tropical Atlantic Ocean along 38°W, J. Geophys. Res., 109, C03052, doi: 10.1029/2003JC002111.

Foltz, G., J. Carton, and E. P. Chassignet (2004b), Tropical instability vortices in the Atlantic Ocean, J. Geophys. Res., 109, C03029, doi: 10.1029/2003JC001942.

Foltz, G. R., and M. J. McPhaden (2010), Interaction between the Atlantic meridional and Niño modes, Geophys. Res. Lett., 37, L18604, doi:10.1029/2010GL044001.

Foltz, G.R., M.J. McPhaden, and R. Lumpkin (2012), A strong Atlantic Meridional Mode event in 2009: The role of mixed layer dynamics, J. Clim., 25, 363-380, doi:10.1175/JCLI-D-11-00150.1.

Fonseca, C., G. Goni, W. E. Johns, and E. J. D. Campos (2004), Investigations of the North Brazil Current retroflection and North Equatorial Countercurrent variability, Geophys. Res. Lett., 31, L21304, doi: 10.1029/2004GL020054.

Frantantoni, D., W. E. Johns, T. L. Townsend, and H. E. Hurlburt (2000), Low latitude circulation and mass transport pathways in a model of the tropical Atlantic Ocean. J. Phys. Oceanogr., 30, 1944–1966.

Garzoli, S. L., and P. L. Richardson (1989), Low-frequency meandering of the Atlantic North Equatorial Countercurrent, J. Geophys. Res.-Oceans, 94(C2), 2079-2090.

Garzoli, S. L. (1992), The Atlantic Equatorial Countercurrent: Models and observations. J. Geophys. Res., 97(C11),17,931-17,946.

Garzoli, S. L., and E. J. Katz (1983), The forced annual reversal of the Atlantic North Equatorial Countercurrent. J. Phys. Oceanogr., 13, 2082-2090.

Giarolla, E., P. Nobre, M. Malagutti, and L. P. Pezzi (2005), The Atlantic Equatorial Undercurrent: PIRATA observations and simulations with GFDL Modular Ocean Model at CPTEC, Geophys. Res. Lett., 32, L10617, doi:10.1029/2004GL022206.

Gilson, J., D. Roemmich, B. Cornuelle, and L.-L. Fu (1998), Relationship of TOPEX/Poseidon altimetric height to steric height and circulation in the North Pacific, J. Geophys. Res., 103(C12), 27,947–27,965, doi:10.1029/98JC01680.

Goes, M., and I. Wainer (2003), Equatorial Currents transport changes for extreme warm and cold events in the Atlantic Ocean, Geophys. Res. Lett., 30 (5), doi: 10.1029/2002GL015707.

Goes, M., R. Molinari, I. C. A. Silveira, and I. Wainer (2005), Retroflections of the North Brazil Current during February 2002, Deep Sea Res. Part 1, 52, 3, 647-667, doi: 10.1016/j.dsr.2004.10.010.

Goldenberg, S. B., C. Landsea, A. M. Mestas-Nunez, and W. M. Gray (2001), The recent increase in Atlantic hurricane activity, Science, 293, 474– 479.

Goni, G., and Baringer, M. (2002), Surface currents in the tropical Atlantic across high density XBT line AX08, Geophys. Res. Lett. 29(24), doi: 10.1029/2002GL015873.

Grodsky, S. A., J. A. Carton, C. Provost, J. Servain, J. A. Lorenzzetti, and M. J. McPhaden (2005), Tropical instability waves at 0ºN, 23ºW in the Atlantic: A case study using Pilot Research Moored Array in the Tropical Atlantic (PIRATA) mooring data, J. Geophys. Res., 110, C08010, doi:10.1029/2005JC002941.Guinehut, S., P.-Y. Le Traon, and G. Larnicol (2006), What can we learn from Global Altimetry/Hydrography comparisons?, Geophys. Res. Lett., 33, L10604.

Hanawa, K., P. Raul, R. Bailey, A. Sy, and M. Szabados (1995), A new depth-time equation for Sippican or TSK T-7, T-6 and T-4 expendable bathythermographs (XBT), Deep-Sea Res. I, 42, 1423-1451.

Hazeleger, W., P. de Vries, and Y. Friocourt (2003), Sources of the Equatorial Undercurrent in the Atlantic in a high-resolution ocean model, J. Phys. Oceanogr., 33, 677-693.Hisard, P., and C. Henin, (1987), Response of the Equatorial Atlantic Ocean to the 1983-1984 wind from the Programme Francais Ocean et Climat Dans l'Atlantique Equatorial cruise data set, J. Geophys. Res., 92, C4, 3759-3768.

Hormann, V., and P. Brandt (2007), Atlantic Equatorial Undercurrent and associated cold tongue variability, J. Geophys. Res., 112, C06017, doi:10.1029/2006JC003931.

Hormann, V., R. Lumpkin and G. Foltz (2012), Interannual North Equatorial Countercurrent variability and its relation to Tropical Atlantic climate modes, J. Geophys. Res., 117, C04035, doi:10.1029/2011JC007697.

Hua, B. L., F. Marin, and R. Schopp (2003), Three-dimensional dynamics of the subsurface countercurrents and equatorial thermostad. Part I: Formulation of the problem and generic properties, J. Phys. Oceanogr., 33, 2588–2609.

Hüttl-Kabus, S., and C. W. Böning (2008), Pathways and variability of the off-equatorial undercurrents in the Atlantic Ocean, J. Geophys. Res. - Oceans, 113, C10018, Doi: 10.1029/2007JC004700.

Jochum, M., P. Malanotte-Rizzoli, and A. Busalacchi (2003), Tropical instability waves in the Atlantic Ocean, Ocean Modell., 7, 146–163, doi:10.1016/S1463-5003(03)00042-8.

Jochum, M., and P. Malanotte-Rizzoli (2004), A new theory for the generation of the equatorial subsurface undercurrents, J. Phys. Oceanogr., 34, 755–771.

Johnson, G. C., and D. W. Moore (1997), The Pacific subsurface countercurrents and an inertial model, J. Phys. Oceanogr., 27(11), 2448–2459.

Katz, E. J. (1987), Seasonal response of the sea surface to wind in the equatorial Atlantic, J. Geophys. Res., 92, 1885–1893.

Katz, E. J., and S. Garzoli(1982) Response of the western equatorial Atlantic Ocean to an annual wind cycle, J. Mar. Res., 40, 307–327.

Katz, E. J. (1993), An interannual study of the Atlantic North Equatorial Countercurrent, J. Phys. Oceanogr., 23, 1, 116-123.

Lagerloef, G., G. T. Mitchum, R. B. Lukas, and P. Niiler (1999), Tropical Pacific near surface currents estimated from altimeter, wind and drifter data, J. Geophys. Res., 104, 23,313-23,326.

Le Traon P.-Y., F. Nadal, N. Ducet (1998), An improved mapping method of multisatellite altimeter data, J. Atmos. Oceanic Technol., 15, 522-533, doi:10.1029/2005GL025551.

Lumpkin, R. and S. L. Garzoli (2005), Near-surface circulation in the tropical Atlantic Ocean, Deep-Sea Res., Part I, 52(3), 495-518.

Ma, H. (1996), The dynamics of North Brazil Current retroflection eddies, J. Mar. Res., 54, 35–53.

Marin, F., F. Schopp, and B. L. Hua (2003), Three-dimensional dynamics of the subsurface countercurrents and equatorial thermostad. Part II: Influence of the large-scale ventilation and equatorial winds, J. Phys. Oceanogr., 33, 2610– 2626.

Metcalf, W., and M. C. Stalcup (1967), Origin of the Atlantic Equatorial Undercurrent, J. Geophys. Res., 72(20), 4959– 4975.

McCarthy, M. C., L. D. Talley, and D. Roemmich (2000), Seasonal to interannual variability from expendable bathythermograph and TOPEX/Poseidon altimeter data in the South Pacific subtropical gyre, J. Geophys. Res., 105(C8), 19,535–19,550, doi:10.1029/2000JC900056.

Moore, D. W., and S. G. H. Philander (1977), Modelling of the tropical oceanic circulation. The Sea, E. D. Goldberg, Ed., Marine Modelling, Vol. 6, Wiley and Sons, 319–361.

Mayer, D., R. L. Molinari, and M. O. Baringer (2001), Transition regions and their role in the relationship between sea surface height and subsurface temperature structure in the Atlantic Ocean, Geophys. Res. Lett., 28, 20, 3943-3946.

McCreary, J. P., P. Lu, and Z. Yu (2002), Dynamics of the Pacific subsurface countercurrents, J. Phys. Oceanogr., 32, 2379–2404.

Menkes, C. E., S. C. Kennan, P. Flament, Y. Dandonneau, S. Masson, B. Biessy, E. Marchal, G. Eldin, J. Grelet, Y. Montel, A. Morlière, A. Lebourges-Dhaussy, C. Moulin, G. Champalbert, and A. Herbland (2002), A whirling ecosystem in the equatorial Atlantic, Geophys. Res. Lett., 29, 1553, doi:10.1029/2001GL014576.

Moore, D. W., and S. G. Philander (1986), Modelling of the tropical Atlantic circulation. *The Sea*, E. D. Goldberg et al., Eds., Marine Modeling, Vol. 6, John Willey and Sons, 319-361.

Moura, A.D., and J. Shukla (1981), On the dynamics of Droughts in Northeast Brazil—observations, theory and numerical experiments with a general-circulation model. J. Atmos. Sci. 38, 2653–2675.

Nobre, P., and J. Shukla (1996), Variations of sea surface temperature, wind stress and rainfall over the tropical Atlantic and South America, J. Clim., 9, 2464– 2479.

Pedlosky, J. (1988), Entrainment and the Termination of the Equatorial Undercurrent, J. Phys. Oceanogr., 18, 880–886.

Peterson, R. G., and L. Stramma (1991), Upper-level circulation in the South Atlantic Ocean, Prog. Oceanogr., 26, 1-73.

Philander, S. G. H., and R. C. Pacanowski (1986), A model of the seasonal cycle in the tropical Atlantic Ocean, J. Geophys. Res., 91(C12), 14,192–14,206.

Phillips, H. E., and S. R. Rintoul (2002), A mean synoptic view of the subantarctic front south of Australia, J. Phys. Oceanogr., 32(5), 1536-1553.

Pond, S. and G. Pickard (1983), Introductory Dynamical Oceanography, 2nd Ed., Pergamon Press Inc., NY 10523, USA.

Reverdin, G., P. Rual, Y. du Penhoat, and Y. Gouriou (1991), Vertical structure of the seasonal cycle in the central equatorial Atlantic Ocean: XBT sections from 1980 to 1988, J. Phys. Oceanogr., 21, 277-291.

Reynolds, R. W., N. A. Rayner, T. M. Smith, D. C. Stokes, and W. Wang (2002), An improved in situ and satellite SST analysis for climate, J. Clim., 15, 1609-1625.

Richardson, P.L., and D. Walsh (1986), Mapping climatological seasonal variations of surface currents in the tropical Atlantic using ship drifts, J. Geophys. Res., 91, 10537-10550.

Richardson, P., and Reverdin, G., (1987), Seasonal cycle of velocity in the Atlantic NECC as measured by surface drifters, current meters and ship drifts. J. Geophys. Res., 92, 3691–3708.

Richardson, S. Arnault, S. Garzoli, and J. G. Bruce, (1992), Annual cycle of the Atlantic North Equatorial Countercurrent. Deep-Sea Res., 39, 997–1014.

Ridgway, K. R., R. C. Coleman, R. J. Bailey, and P. Sutton (2008), Decadal variability of East Australian Current transport inferred from repeated high-density XBT transects, a CTD survey and satellite altimetry, J. Geophys. Res., 113, C08039, doi:10.1029/2007JC004664.

Rintoul, S. R., S. Sokolov, and J. Church (2002), A 6 year record of baroclinic transport variability of the Antarctic Circumpolar Current at 140°E derived from expendable bathythermograph and altimeter measurements, J. Geophys. Res., 107(C10), 3155, doi:10.1029/2001JC000787.

Rio, M. H., S. Guinehut, and G. Larnicol (2011), New CNES-CLS09 global mean dynamic topography computed from the combination of GRACE data, altimetry, and in situ measurements, J. Geophys. Res., 116, C07018, doi:10.1029/2010JC006505.

Roemmich, D., and J. Gilson (2001), Eddy Transport of Heat and Thermocline Waters in the North Pacific: A Key to Interannual/Decadal Climate Variability?, J. Phys. Oceanogr., 31, 675–687.

Rowe, G. D., E. Firing, and G. C. Johnson (2000), Pacific equatorial subsurface countercurrent velocity, transport, and potential vorticity, J. Phys. Oceanogr., 30, 1172– 1187.

Schott, F., L. Stramma, and J. Fischer (1995), The warm water inflow into the western tropical Atlantic boundary regime, spring 1994, J. Geophys. Res., 100, 24745–24760.

Schott, F., J. Fisher, and L. Stramma (1998), Transports and pathways of the upper-layer circulation in the western tropical Atlantic, J. Phys.l Oceanogr., 28, 1904–1928.

Schott, F. A., M. Dengler, P. Brandt, K. Affler, J. Fischer, B. Bourlès, Y. Gouriou, R. L. Molinari, and M. Rhein (2003), The zonal currents and transports at 35°W in the tropical Atlantic, Geophys. Res. Lett., 30, 7, 1349, doi:10.1029/2002GL016849.

Schott, F., J. McCreary, and G. Johnson (2004), Shallow Overturning Circulations of the Tropical-Subtropical Oceans, In Earth Climate: The Ocean-Atmosphere Interaction, C. Wang, S.-P. Xie and J.A. Carton (eds.), AGU Geophysical Monograph Series, 147, 261–304.

Servain, J., I. Wainer, J.P. McCreary, and A. Dessier (1999), A relationship between the equatorial and meridional modes of climatic variability in the tropical Atlantic, Geophys. Res. Lett., 26(4), 485-488, doi:10.1029/1999GL900014.

Stramma, L. S., and M. England (1999), On the water masses and mean circulation of the South Atlantic. J. Geophys. Res., 104, 20,863-20,833.

Stramma, L., S. Hüttl, and J. Schafstall (2005), Water masses and currents in the upper tropical northeast Atlantic off northwest Africa, J. Geophys. Res., 110, C12006, doi:10.1029/2005JC002939.

Sutton, R. T. and D. L. R. Hodson (2005), Atlantic Ocean forcing of North American and European summer climate. Science, 309 (5731), 115-118, doi: 10.1175/JCLI4038.1.

Tabata, S., B. Thomas, and D. Ramsden (1986), Annual and interannual variability of steric sea level along line P in the northeast Pacific ocean, J. Phys. Oceanogr., 16, 1378-1398.

Torrence, C., and G. P. Compo (1998), A Practical Guide to Wavelet Analysis, Bulletin of the American Meteorological Society, 79, 1, 61-78. Software available at URL: http://atoc.colorado.edu/research/wavelets/.

Urbano, D. F., M. Jochum, and I. C. A. Silveira (2006), Rediscovering the second core of the Atlantic NECC, Ocean Modell.,12, 1–15, doi:10.1016/j.ocemod.2005.04.003.

Voituriez, B. (1981), Les sous courants equatoriaux Nord et Sud et la Formation des domes thermiques tropicaux, Oceanolog. Acta., 5, 497-506.

Wacongne, S. (1989). Dynamical regimes of a fully nonlinear stratified modelof the Atlantic equatorial undercurrent. J. Geophys. Res., 94, 4810–15.

Weisberg, R. H., J. H. Hickman, T. Y. Tang, and T. J. Weingartner (1987), Velocity and temperature observations during the Seasonal Response of the Equatorial Atlantic Experiment at 0°,28°W, J. Geophys. Res., 92, 5061-5075.

Weisberg, R., and T. Weingartner (1988), Instability waves in the equatorial Atlantic Ocean, J. Phys. Oceanogr., 18, 1641– 1657.

Xie, S.-P., and S.G.H. Philander (1994), A coupled ocean-atmosphere model of relevance to the ITCZ in the eastern Pacific, Tellus, 46A, 340-350.

Yang, J., and T M. Joyce, (2006), Local and Equatorial Forcing of Seasonal Variations of the North Equatorial Countercurrent in the Atlantic Ocean, J. Phys. Oceanogr.,26, 238-254.

Zhang, D., M. J. McPhaden, and W. E. Johns (2003), Observational Evidence for Flow between the Subtropical and Tropical Atlantic: The Atlantic Subtropical Cells, J. Phys. Oceanogr., 33, 1783-1797.

Figure Captions:

Figure 1: a) Root mean square of SLA (cm) in the tropical Atlantic (filled contours), with superimposed AX08 sections: selected sections (black), sections not included in the analysis (gray), and mean of the selected sections (red). b) Probability density function of the averaged longitude between 10°S-10°N for all the AX08 XBT sections. c) Histogram of the monthly distribution of the number of the sections before (blue) and after (red) the selection of the sections that fit into the 68 percentile of b).

Figure 2: Typical temperature (°C) and salinity (psu) distributions for January (a, c) and June (b, d) 2010. Salinity is derived from WOD01 climatological T-S relationships. The mean locations of the eastward currents are marked in (a), and the approximate depths of the water masses are indicated in (c).

Figure 3: Anomalies of surface dynamic height (DH_0', red), with respect to the annual mean of the XBT data, along with corresponding thermosteric (blue) and halosteric (green) components at (a) 4.5°N, (b) the equator, and (c) 4.5°S.

Figure 4: Comparison between SLA and surface dynamic height anomalies (DH_0'): Longitude-time diagrams of (a) SLA, (b) DH_0', and (c) SLA - DH_0'; dots on the right-hand side of (c) mark the realizations of the AX08 XBT transect. (d) Linear fit between DH_0' and SLA.

Figure 5: Correlation at each depth and latitude between surface dynamic height anomalies (DH_0) and: a) density anomalies (σ_θ), and b) dynamic height anomalies (DH'). The thick black lines in b) mark the mean location of the isopycnals σ_θ = 24.5 kg m^{-3} and σ_θ = 26.8 kg m^{-3} that define the upper and lower dynamic layers, respectively.

Figure 6: Mean seasonal cross-sectional velocities derived from XBT data (coloring), with σ_θ = 24.5 kg m^{-3} and σ_θ = 26.8 kg m^{-3} isopycnals overlaid (black lines): (a) Dec, Jan; (b) Mar, Apr, May; (c) Jun, Jul, Aug; and (d) Sep, Oct, Nov. The seasonal-mean absolute surface dynamic height is shown on top of each panel.

Figure 7: Geostrophic transports estimated from the synthetic method (black line with open dots) and from the XBT data (blue dots), with corresponding linear fit between the two transport estimates: (a, b) NECC, (c, d) NEUC, (e, f) SEUC, and (g, h) EUC.

Figure 8: Seasonal cycle of geostrophic transport (Sv), core velocity (cm/s), and latitudinal position (deg): (a, e, i) NECC, (b, f, j) NEUC, (c, g, k) SEUC, and (d, h, l) EUC. Red dots are monthly XBT averages and red line represents the corresponding fit of annual and semi-annual harmonics; green and blue lines mark the average synthetic estimates for the periods 1993-2000 and 2000-2010, respectively. Shown error bars are the standard errors for the synthetic estimates, and the standard error plus fitting error for the XBT data.

Figure 9: Time series and respective wavelet transforms for the monthly (a) NECC transport, (b) NEUC transport, (c) EUC transport, and d) zonal pseudo-wind stress averaged over the region 5°S-5°N/30°W-20°W. Transport time series are generated by the synthetic method. The wavelet power spectra are based on a Morlet transform and regions above the 95% significance level are encircled by black contours, with the bowl-shaped black lines indicating the cone of influence.

Figure 10: a) Instantaneous correlation between the standardized NECC transport anomalies and both SSTA (coloring) and pseudo-wind stress anomalies (vectors). Only the statistically significant values are shown. b) Time series of the standardized NECC transport anomalies (red), SSTA index (blue), and meridional wind index (y-wind, black). The SSTA index is

defined by subtracting the averages over the northern (35°W-17°W/0-7°N) and southern (30°W-15°W/11°S-23°S) boxes as marked in (a), and the wind index is defined as the average of the meridional pseudo-wind stress anomalies in the northern box. c) Lagged correlations of the NECC with the SST (blue) and wind indices (black), with significant values marked with bold lines.

Figure 11: Same as Figure 10, but for NEUC transport anomalies. The SST index (blue) is defined here as the difference between the northern box average over the Guinea Dome region (10°-25°N/15°-35°W) and the southern box average (8°S-5°N/30°W-10°E) as marked in (a), and the y-wind index is defined as the average of meridional pseudo-wind stress anomalies over the northern box.

Tables captions:

Table 1 – Latitudinal and isopycnal ranges used in the volume transport calculations of the Atlantic equatorial eastward currents.

Table 2 – Percentage of the variance of transport, core velocity, and position explained by the annual and semi-annual harmonics for each current using XBT estimates and the synthetic method for the periods 1990-2000 (S/1990-2000) and 2000-2010 (S/2000-2010). The synthetic method is not analyzed for the SEUC.

Figures:

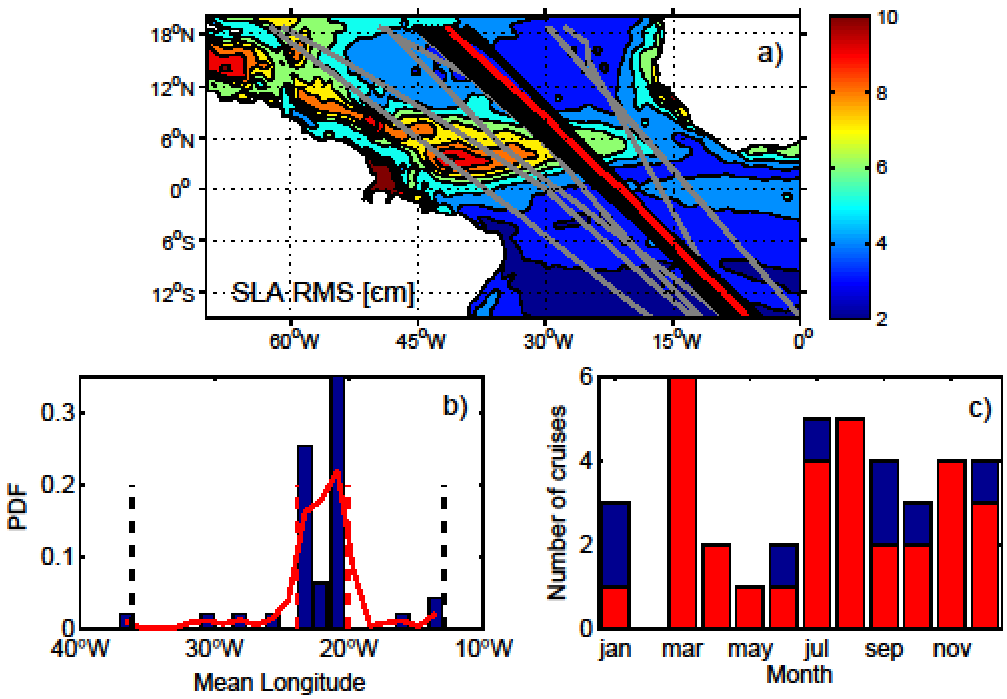

Figure 1: a) Root mean square of SLA (cm) in the tropical Atlantic (filled contours), with superimposed AX08 sections: selected sections (black), sections not included in the analysis (gray), and mean of the selected sections (red). b) Probability density function of the averaged longitude between 10°S-10°N for all the AX08 XBT sections. c) Histogram of the monthly distribution of the number of the sections before (blue) and after (red) the selection of the sections that fit into the 68 percentile of b).

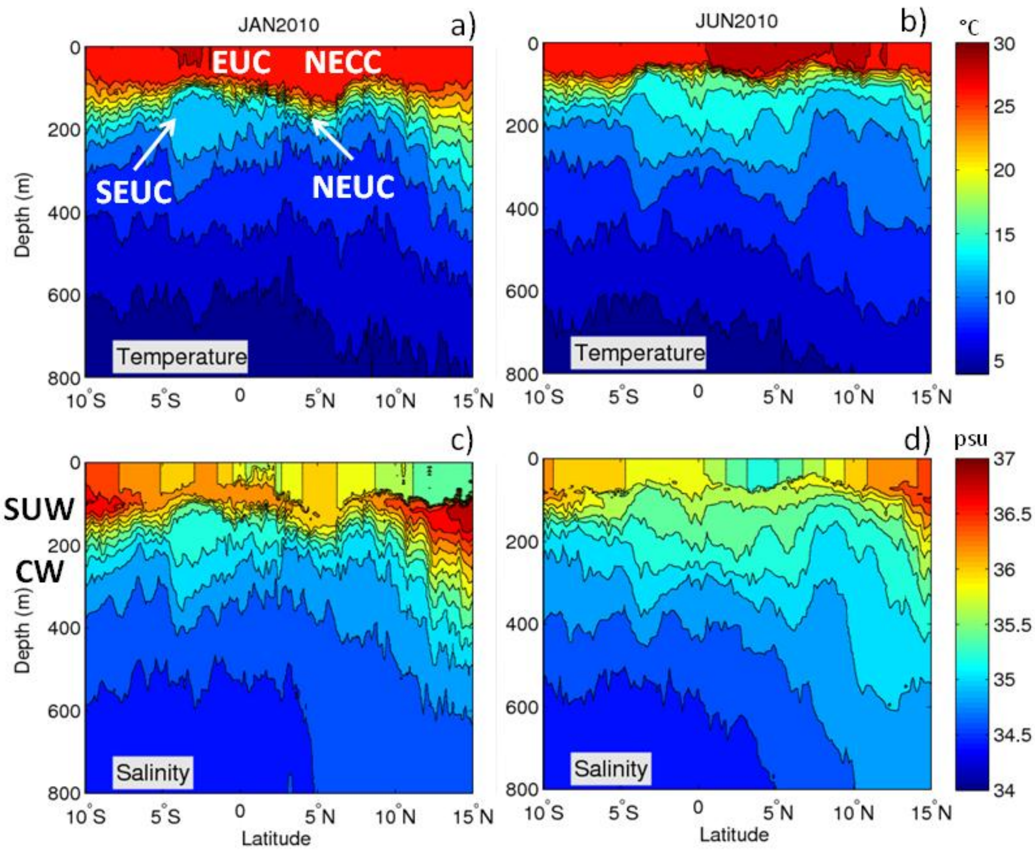

Figure 2: Typical temperature (°C) and salinity (psu) distributions for January (a, c) and June (b, d) 2010. Salinity is derived from WOD01 climatological T-S relationships. The mean locations of the eastward currents are marked in (a), and the approximate depths of the water masses are indicated in (c).

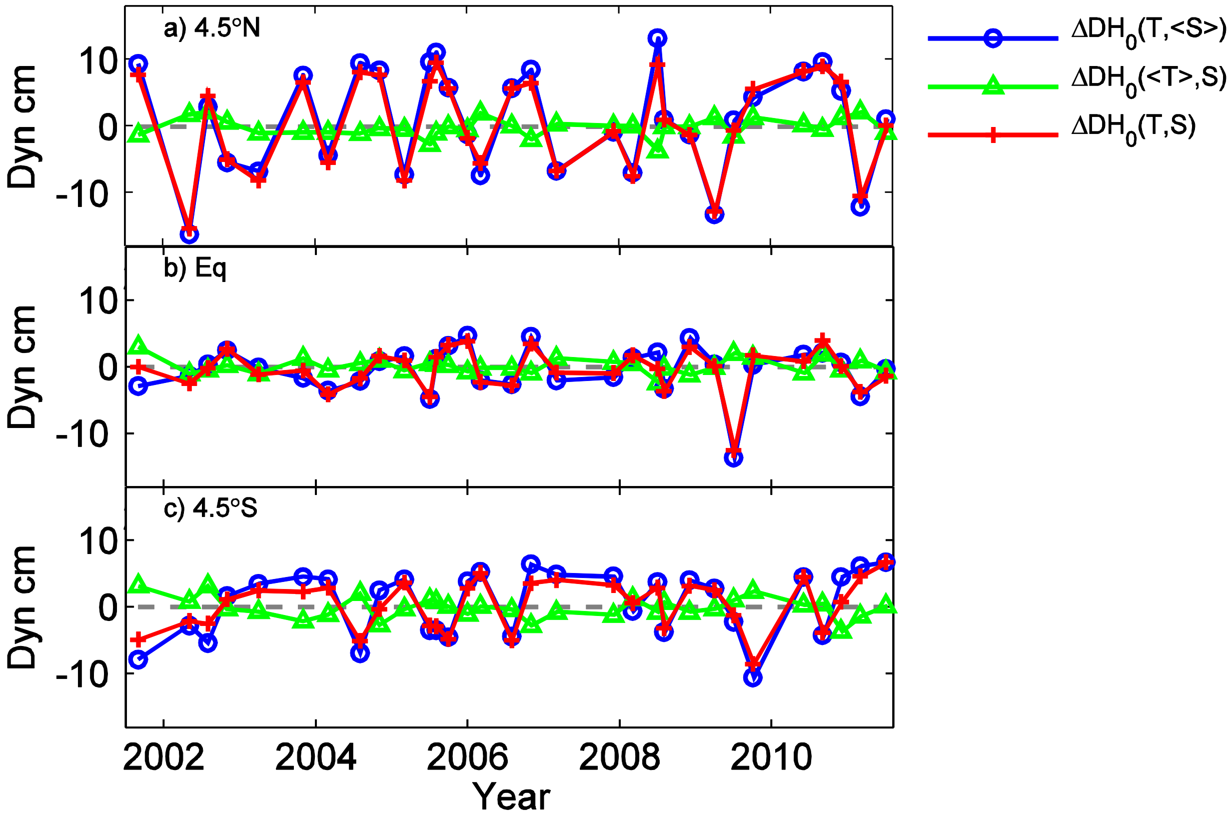

Figure 3: Anomalies of surface dynamic height (DH$_0$', red), with respect to the annual mean of the XBT data, along with corresponding thermosteric (blue) and halosteric (green) components at (a) 4.5°N, (b) the equator, and (c) 4.5°S.

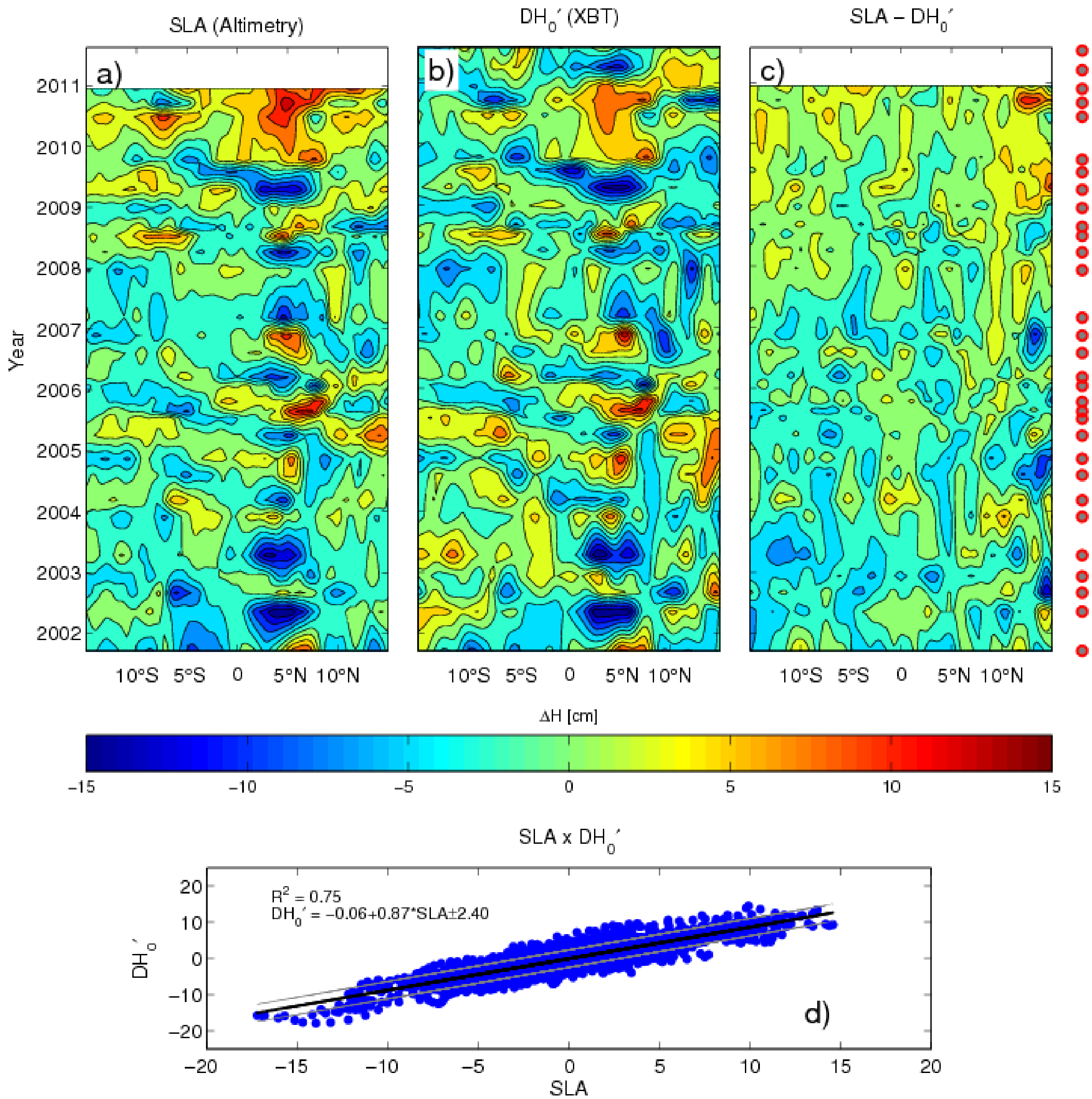

Figure 4: Comparison between SLA and surface dynamic height anomalies (DH_0’): Longitude-time diagrams of (a) SLA, (b) DH_0’, and (c) SLA - DH_0’; dots on the right-hand side of (c) mark the realizations of the AX08 XBT transect. (d) Linear fit between DH_0’ and SLA.

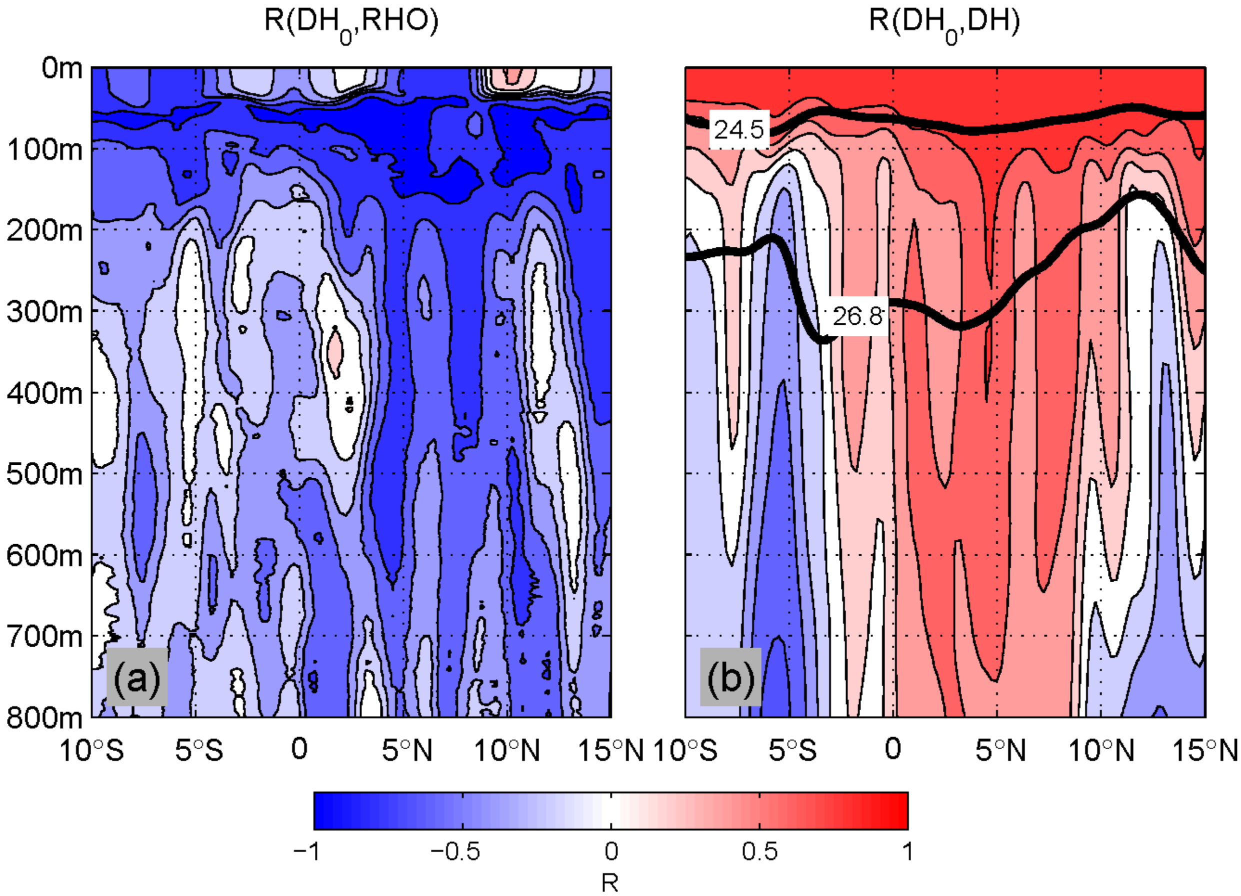

Figure 5: Correlation at each depth and latitude between surface dynamic height anomalies (DH_0) and: a) density anomalies (σ_θ), and b) dynamic height anomalies (DH’). The thick black lines in b) mark the mean location of the isopycnals σ_θ = 24.5 kg m^{-3} and σ_θ = 26.8 kg m^{-3} that define the upper and lower dynamic layers, respectively.

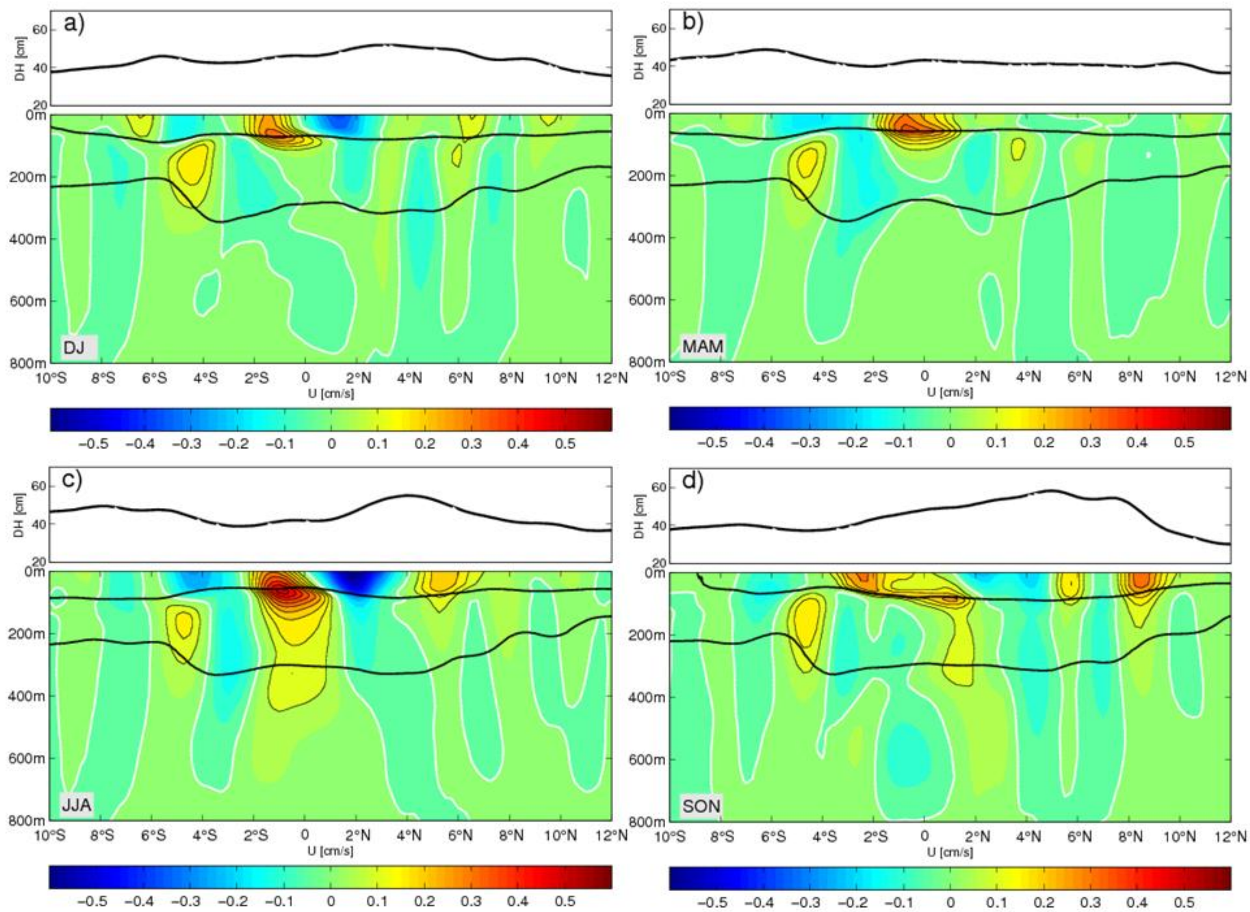

Figure 6: Mean seasonal cross-sectional velocities derived from XBT data (coloring), with σ_θ = 24.5 kg m^{-3} and σ_θ = 26.8 kg m^{-3} isopycnals overlaid (black lines): (a) Dec, Jan; (b) Mar, Apr, May; (c) Jun, Jul, Aug; and (d) Sep, Oct, Nov. The seasonal-mean absolute surface dynamic height is shown on top of each panel.

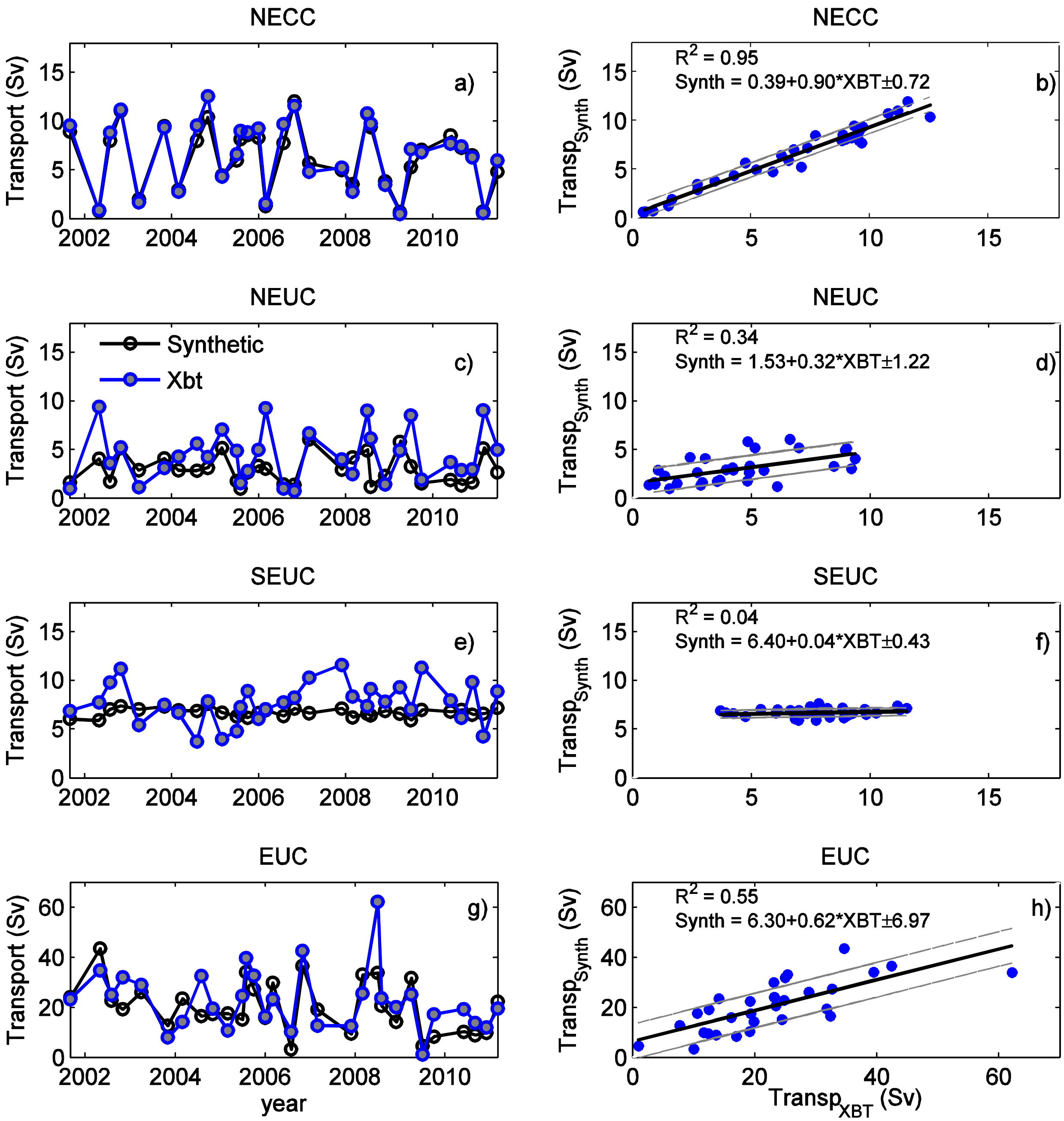

Figure 7: Geostrophic transports estimated from the synthetic method (black line with open dots) and from the XBT data (blue dots), with corresponding linear fit between the two transport estimates: (a, b) NECC, (c, d) NEUC, (e, f) SEUC, and (g, h) EUC.

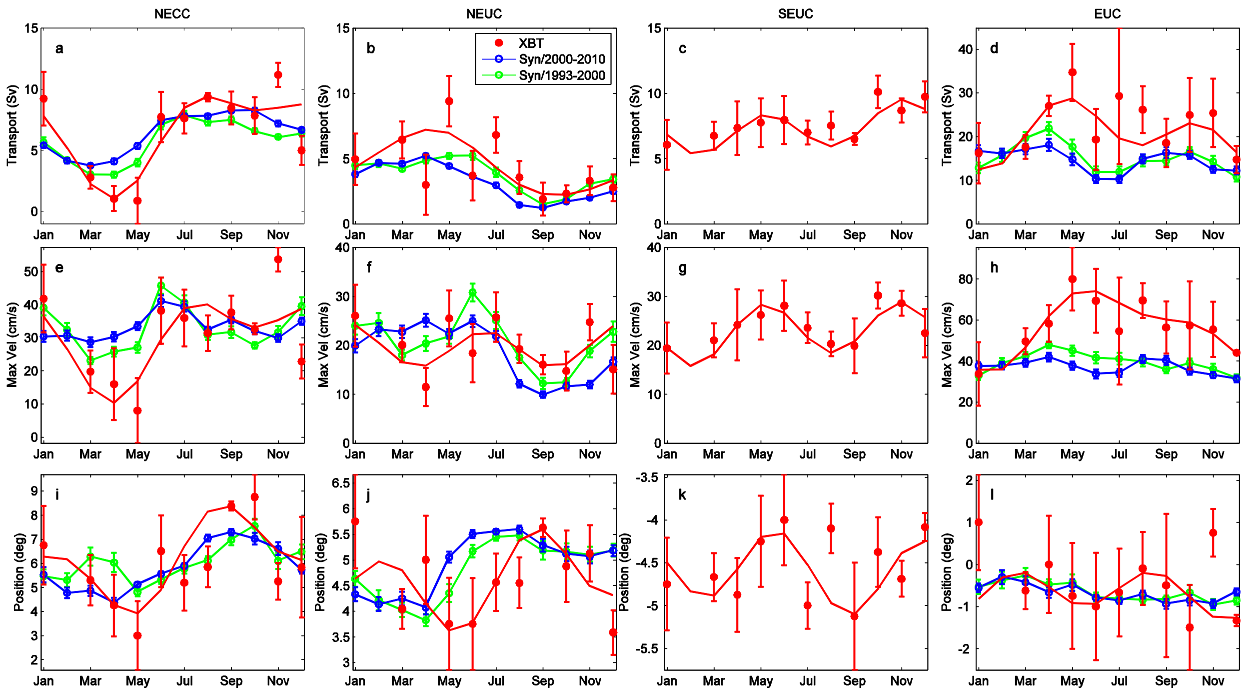

Figure 8: Seasonal cycle of geostrophic transport (Sv), core velocity (cm/s), and latitudinal position (deg): (a, e, i) NECC, (b, f, j) NEUC, (c, g, k) SEUC, and (d, h, l) EUC. Red dots are monthly XBT averages and red line represents the corresponding fit of annual and semi-annual harmonics; green and blue lines mark the average synthetic estimates for the periods 1993-2000 and 2000-2010, respectively. Shown error bars are the standard errors for the synthetic estimates, and the standard error plus fitting error for the XBT data.

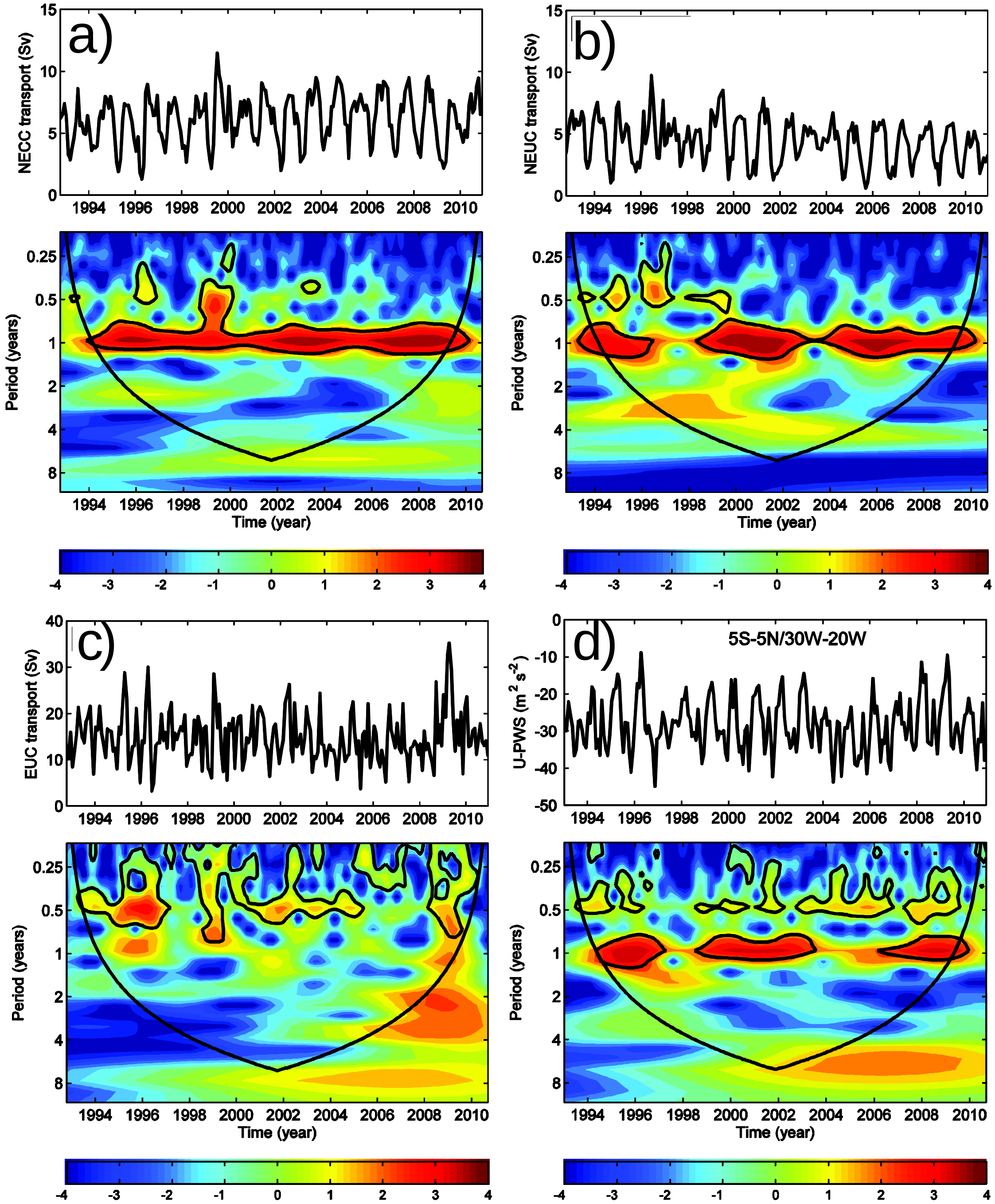

Figure 9: Time series and respective wavelet transforms for the monthly (a) NECC transport, (b) NEUC transport, (c) EUC transport, and d) zonal pseudo-wind stress averaged over the region 5°S-5°N/30°W-20°W. Transport time series are generated by the synthetic method. The wavelet

power spectra are based on a Morlet transform and regions above the 95% significance level are encircled by black contours, with the bowl-shaped black lines indicating the cone of influence.

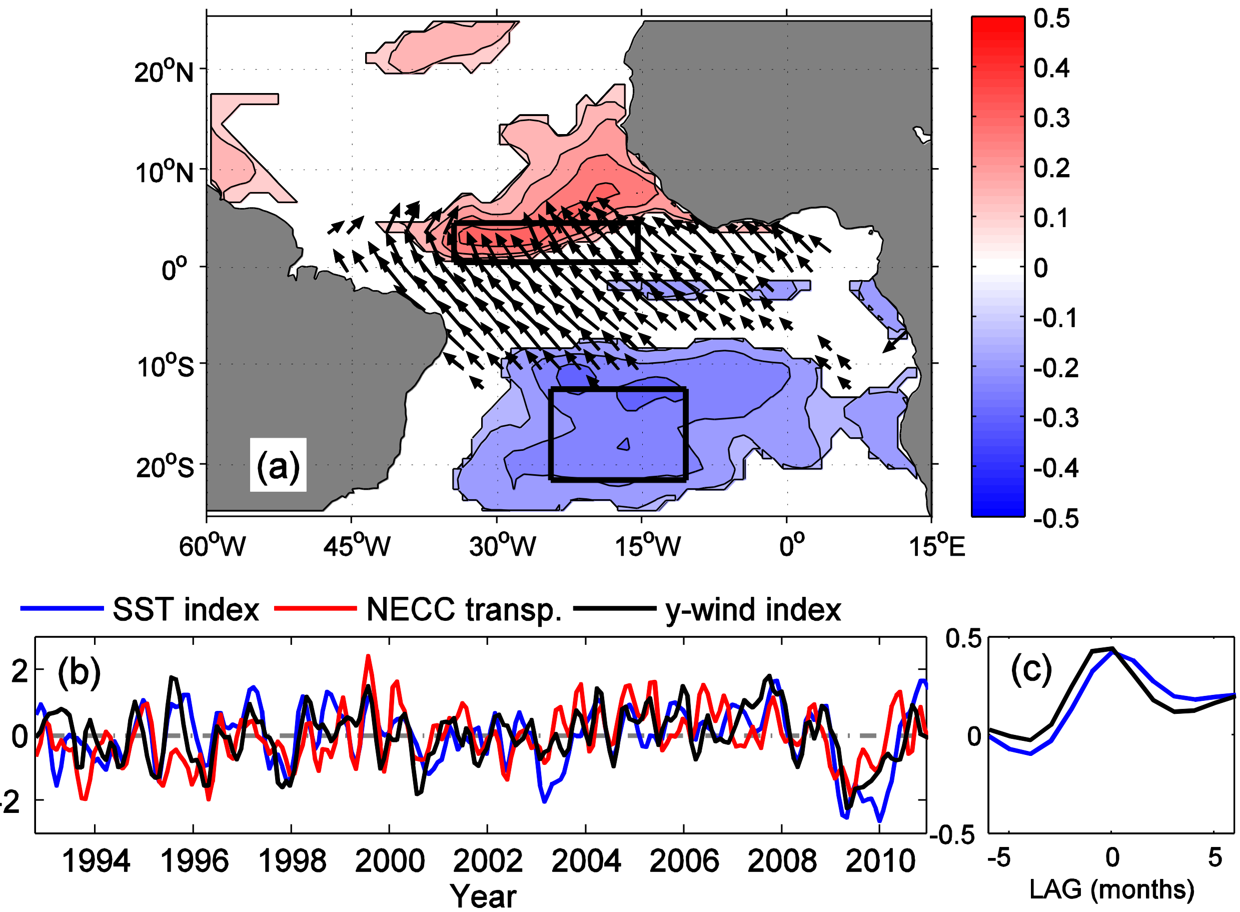

Figure 10: a) Instantaneous correlation between the standardized NECC transport anomalies and both SSTA (coloring) and pseudo-wind stress anomalies (vectors). Only the statistically significant values are shown. b) Time series of the standardized NECC transport anomalies (red), SSTA index (blue), and meridional wind index (y-wind, black). The SSTA index is defined by subtracting the averages over the northern (35°W-17°W/0-7°N) and southern (30°W-15°W/11°S-23°S) boxes as marked in (a), and the wind index is defined as the average of the meridional pseudo-wind stress anomalies in the northern box. c) Lagged correlations of the

NECC with the SST (blue) and wind indices (black), with significant values marked with bold lines.

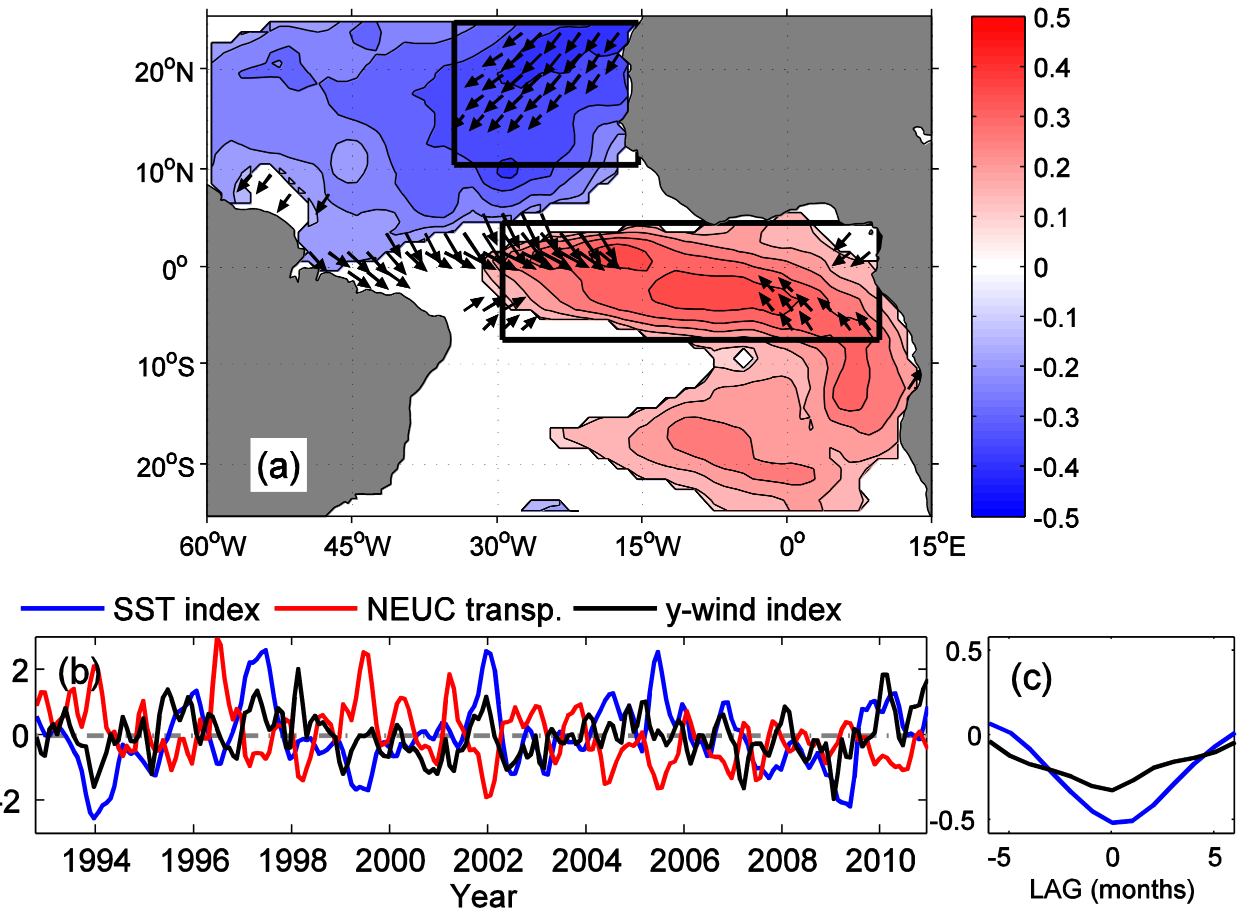

Figure 11: Same as Figure 10, but for NEUC transport anomalies. The SST index (blue) is defined here as the difference between the northern box average over the Guinea Dome region (10°-25°N/15°-35°W) and the southern box average (8°S-5°N/30°W-10°E) as marked in (a), and the y-wind index is defined as the average of meridional pseudo-wind stress anomalies over the northern box.

Table 1: Latitudinal and isopycnal ranges used in the volume transport calculations of the Atlantic equatorial eastward currents.

Current	Latitude	σ_θ (kg m^{-3})
NECC	3°N - 10°N	0 - 24.5
NEUC	3°N - 6°N	24.5 - 26.8
EUC	2.5°S - 2.5°N	0 - 26.8
SEUC	6°S - 3°S	24.5 - 26.8

Table 2: Percentage of the variance of transport, core velocity, and position explained by the annual and semi-annual harmonics for each current using XBT estimates and the synthetic method for the periods 1990-2000 (S/1990-2000) and 2000-2010 (S/2000-2010). The synthetic method is not analyzed for the SEUC.

Current	Data	Transport (%)		Core Velocity (%)		Position (%)	
		Annual	Semi-annual	Annual	Semi-annual	Annual	Semi-annual
NECC	XBT	58	13	41	20	52	19
	S/1990-2000	78	17	5	66	64	14
	S/2000-2010	93	3	31	23	95	1
NEUC	XBT	63	1	1	35	22	41
	S/1990-2000	75	21	23	64	80	17
	S/2000-2010	99	1	83	5	76	13
SEUC	XBT	14	90	8	92	5	60
EUC	XBT	24	40	72	16	2	21
	S/1990-2000	28	64	79	22	70	15
	S/2000-2010	19	68	13	54	69	10